Icarus 262 (2015) 14–29

Contents lists available at ScienceDirect

Icarus

journal homepage: www.elsevier.com/locate/icarus

Monte-Carlo simulation of Callisto's exosphere

A. Vorburger [a,*], P. Wurz [b], H. Lammer [c], S. Barabash [d], O. Mousis [e]

[a] Dept. of Earth and Planetary Sciences, Division of Physical Sciences, American Museum of Natural History, New York 10024, USA
[b] Physikalisches Institut, University of Bern, Bern, Switzerland
[c] Austrian Academy of Sciences, Graz, Austria
[d] Swedish Institute of Space Physics, Kiruna, Sweden
[e] Aix Marseille Université, CNRS, LAM (Laboratoire d'Astrophysique de Marseille) UMR 7326, 13388 Marseille, France

ARTICLE INFO

Article history:
Received 10 March 2015
Revised 22 July 2015
Accepted 30 July 2015
Available online 11 August 2015

Keyword:
Callisto
Atmospheres, composition
Jupiter, satellites
Satellites, atmospheres

ABSTRACT

We model Callisto's exosphere based on its ice as well as non-ice surface via the use of a Monte-Carlo exosphere model. For the ice component we implement two putative compositions that have been computed from two possible extreme formation scenarios of the satellite. One composition represents the oxidizing state and is based on the assumption that the building blocks of Callisto were formed in the protosolar nebula and the other represents the reducing state of the gas, based on the assumption that the satellite accreted from solids condensed in the jovian sub-nebula. For the non-ice component we implemented the compositions of typical CI as well as L type chondrites. Both chondrite types have been suggested to represent Callisto's non-ice composition best. As release processes we consider surface sublimation, ion sputtering and photon-stimulated desorption. Particles are followed on their individual trajectories until they either escape Callisto's gravitational attraction, return to the surface, are ionized, or are fragmented. Our density profiles show that whereas the sublimated species dominate close to the surface on the sun-lit side, their density profiles (with the exception of H and H_2) decrease much more rapidly than the sputtered particles. The Neutral gas and Ion Mass (NIM) spectrometer, which is part of the Particle Environment Package (PEP), will investigate Callisto's exosphere during the JUICE mission. Our simulations show that NIM will be able to detect sublimated and sputtered particles from both the ice and non-ice surface. NIM's measured chemical composition will allow us to distinguish between different formation scenarios.

1. Introduction

The core accretion model is the favored concept to explain the formation of giant planets in the Solar System (Pollack et al., 1996; Alibert et al., 2005a, 2013; Mordasini et al., 2014). According to this scenario, the formation of a giant planet comprises five steps: (i) Cloud collapse and star-disk formation, (ii) Dust growth and planetesimal formation, (iii) Planetary embryo growth, (iv) Gas capture and gap opening, and (v) Long term gravitational evolution of the planet (Pollack et al., 1996; Alibert et al., 2005a, 2013; Mordasini et al., 2014).

In the framework of this model, the regular jovian satellites are formed within a sub-nebula generated by the material (gas and gas-coupled solids) accreted by the giant planet during the last phase of its formation (Coradini and Magni, 1984; Lubow et al., 1999; Canup and Ward, 2002, 2006). The formation circumstances of the Galilean satellites are still poorly understood and strongly depend on the thermodynamic conditions encountered within the jovian sub-nebula prior to their accretion. The building blocks of the jovian satellites may have initially formed in the feeding zone of Jupiter before being embedded within the sub-nebula. If the sub-nebula were cold enough to avoid the vaporization of ices at the formation epochs and locations of Ganymede and Callisto, they may have assembled from these building blocks whose chemical and isotopic compositions would have been set by their condensation conditions in the protosolar nebula (Mousis and Gautier, 2004; Alibert et al., 2005b; Mousis and Alibert, 2006). This scenario is consistent with the formation of Saturn's satellite Enceladus whose D/H ratio in H_2O has been measured in its plumes by the Cassini spacecraft and found similar to the value measured in Oort Cloud comets ($D/H \sim 3 \times 10^{-4}$) (Waite et al., 2009; Kavelaars et al., 2011). Indeed, if Enceladus were accreted from building blocks condensed within an initially warm Saturn's sub-nebula, then the D/H ratio in the H_2O accreted by the satellite would have been close to the protosolar value, due to an isotopic

---

[*] Corresponding author.
E-mail address: avorburger@amnh.org (A. Vorburger).

http://dx.doi.org/10.1016/j.icarus.2015.07.035
0019-1035/© 2015 Elsevier Inc. All rights reserved.

exchange between water and hydrogen in the gas phase of the sub-nebula prior to satellitesimals condensation (Horner et al., 2008; Kavelaars et al., 2011). In this scenario, the building blocks of Io and Europa would have been partly devolatilized during their migration within the sub-nebula (Alibert et al., 2005b). Alternatively, Io and Europa could have formed volatiles-rich but would have been progressively devolatilized with time due to tidal dissipation (Schubert et al., 2010). An opposite scenario is the formation of Galilean satellites from building blocks condensed in an initially warm and dense jovian sub-nebula (Prinn and Fegley, 1981; Prinn and Fegley, 1989). This would be the case if the satellites formed at early epochs of the sub-nebula's life when it was dense and hot enough to vaporize any solid entering from the protosolar nebula (Alibert et al., 2005b; Alibert and Mousis, 2007). In this case, the chemical and isotopic composition of the ices formed in this environment would be drastically different from those condensed in the protosolar nebula.

Under these circumstances, measuring the internal composition of the jovian satellites would bring important constraints on their formation conditions within the sub-nebulae, as well as on the thermodynamic conditions that took place in the protosolar nebula at the epoch of the giant planets formation. If convective plumes come close enough to the satellite's surface, they can supply fresh material representing the bulk compositions of the satellites to the surface, identification of which could thus help shed light on the satellite's formation condition.

The JUpiter ICy moons Explorer (JUICE) mission (Grasset et al., 2013), which is currently in implementation by the European Space Agency (ESA), is intended for the detailed investigations of Jupiter and its system in all their inter-relations and complexity. JUICE will also investigate Europa, Callisto and Ganymede, with particular emphasis on Ganymede. Among the planned scientific investigations of JUICE are explorations of the chemical composition of the Galilean moons. The Particle Environment Package (PEP) suite contains instruments for the comprehensive measurements of electrons, ions and neutrals (Barabash et al., 2013). The Neutral and Ion Mass spectrometer (NIM), which is part of the PEP instrument suite, will measure the neutral and ion composition of the exospheres of these moons during flybys and in orbit of Ganymede. In addition to the NIM/PEP instrument there are several other instrument that will be performing exospheric measurements on JUICE, which are JUICE-MAJIS (Langevin et al., 2013), SWI (Hartogh et al., 2013), UVS (Gladstone et al., 2013), and RPWI (Wahlund et al., 2013). It is assumed that Callisto is not fully differentiated (e.g., Nagel et al. (2004) and references therein) and that its surface composition consist of about half ice and half mineral contents. Thus, composition measurements at Callisto offer the unique opportunity to measure the full spectrum of building blocks of the Jupiter system.

Various physical processes are acting on the surfaces of Jupiter's icy moons to promote material from the surface into the exosphere. These are thermal desorption (sublimation), photon stimulated desorption (PSD), ion-induced sputtering, and micrometeorite impact vaporization. Sputtering releases all species present on the surface more or less stoichiometrically into the exosphere, allowing to derive the chemical composition of the surface from these measurements.

In this paper, we model Callisto's exospheric density profiles ab initio from its ice as well as non-ice surface via the use of a Monte-Carlo exosphere model. Our Monte-Carlo model assumes that the particles travel on unhindered trajectories, as is only in an exosphere the case. Observations published while this paper was under revision imply that Callisto's exosphere might be collisional rather than collision-less, though (Cunningham et al., 2015). A follow-up study will thus have to determine the influence this might have. We investigate two ice and two non-ice materials each, and determine whether they can be distinguished based on exospheric measurements (i.e., measurements taken at a certain altitude). In addition, we examine NIM's measurement capabilities of Callisto's exosphere as computed from our model.

The paper is outlined as follows: Section 2 presents previously conducted observations of Callisto's surface and atmospheric composition. Section 3 presents Callisto's surface composition as modeled in this paper, the jovian plasma environment in which we positioned Callisto, and details of the Monte Carlo Model used to calculate the exospheric density profiles from the given surface compositions and plasma environment conditions. The exospheric densities as computed from our model are presented in Section 4 whereas a thorough discussion and conclusion of the density profiles and NIM's measurement capabilities are provided in Sections 5 and 6.

2. Callisto composition observations

2.1. Surface composition observations

From ground based observations, it was known as early as in the 1920s that Callisto's surface is not homogeneous (Stebbins and Jacobsen, 1928). Its leading hemisphere was discovered to be darker and redder than the trailing hemisphere, contrary to the other Galilean satellites (Moore et al., 2004). Towards the end of the 1970s, spacecraft observations by Voyager 1 and 2 shed further light onto Callisto's geological surface, which was discovered to be heavily cratered (Smith et al., 1979). The Voyager measurements also allowed precise determination of Callisto's bulk density, which indicates that Callisto is a mixture of rock and ice. During the Galileo mission Callisto was analyzed with high spectral resolution at near-infrared and ultraviolet wavelengths (Greeley et al., 2000). Two distinct absorption bands in the reflectance spectra were attributed to the presence of carbon dioxide and sulfur dioxide (Carlson et al., 1996; McCord et al., 1998), both of which are distributed asymmetrically over Callisto's surface: Whereas the trailing hemisphere seems to be enriched in carbon dioxide, the leading hemisphere has more sulfur dioxide (Hibbitts et al., 2000). In addition, a weak (in comparison to Ganymede) O_2 band was observed on Callisto's trailing hemisphere by the Ohio State University CCD spectrograph at the Lowell Observatory Perkins 72 in. telescope (Spencer and Calvin, 2002), though no O_2 abundance was inferred thereof.

2.2. Atmosphere composition observations

Up until very recently, only carbon dioxide had been directly observed in Callisto's atmosphere. With the Galileo Near-Infrared Mapping Spectrometer (NIMS) a CO_2 signal up to 100 km above the surface was recorded (Carlson, 1999). Comparison with a theoretical altitude profile led to an inferred surface pressure of $7.5 \cdot 10^{-7}$ Pa (7.5 pbar) and a temperature of 150 ± 50 K, which is close to the noon surface temperature of Callisto. The authors derived an atmospheric CO_2 scale height of 23 km, an exospheric surface number density of $N_0 \approx 4 \times 10^8\ \mathrm{cm}^{-3}$ and a vertical column abundance of $N_C \approx 8 \times 10^{14}\ \mathrm{cm}^{-2}$.

During the same mission, using the radio occultation technique, the first measurements of an ionospheric layer above Callisto's sunlit trailing hemisphere were conducted (Kliore et al., 2002). The observations yielded peak electron densities of 15,300 and 17,400 cm^{-3} at altitudes of 27.2 and 47.6 km, respectively. The photo-ionization of the observed neutral CO_2 atmosphere is insufficient to produce the observed electron densities, though. The authors therefore propose the existence of a neutral atmosphere consisting primarily of O_2 and infer O_2 surface densities of

$N_0 = (1\text{–}3) \times 10^{10}\ \mathrm{cm}^{-3}$ and column densities of $N_C = (3\text{–}4) \times 10^{16}\ \mathrm{cm}^{-2}$. Liang et al. (2005) modeled photochemical reactions in an O_2-rich atmosphere ($N_0 = 7 \times 10^9\ \mathrm{cm}^{-3}$) which successfully reproduced the observed electron profile. The atomic oxygen produced from O_2 photo-dissociation is 2 orders of magnitude larger than upper limits derived from Space Telescope Imaging Spectrograph measurements aboard the Hubble Space Telescope (Strobel et al., 2002), though. The authors therefore propose that H_2O vapor needs to be present in the atmospheres, the OH radicals of which can remove the mentioned O atoms.

First evidence for the existence of an O_2 atmosphere was most recently found by the Hubble Space Telescope Cosmic Origins Spectrograph: Observations of Callisto's leading hemisphere showed, for the first time, variable-strength atomic oxygen emissions in both the 1304 Å triplet and the 1356 Å doublet (Cunningham et al., 2015). The 1356 Å/1304 Å emission ratio from Callisto's disk favors dissociative excitation of O_2, suggesting that O_2 is the dominant atmospheric component rather than other possible oxygen-bearing alternatives. Their detection yields an O_2 column density of $N_C \approx 4 \times 10^{15}\ \mathrm{cm}^{-2}$ on the leading hemisphere, implying that Callisto's atmosphere is collisional rather than collision-less. The authors also mention that longitudinal variations in published densities of ionospheric electrons suggest that on the unobserved trailing hemisphere the densities might be an order of magnitude larger. In addition to the O_2, their measurements hint to an atomic oxygen atmosphere with a density of up to $10^4\ \mathrm{cm}^{-3}$ at the exobase.

3. Model

Several processes are responsible for the input and loss of atomic species to and from planetary exospheres (Wurz and Lammer, 2003; Killen et al., 2007; Wurz et al., 2007). The main release processes acting on Callisto are (1) thermal desorption/sublimation, (2) ion induced sputtering, (3) and photon-stimulated desorption. The sublimated flux is a function of Callisto's surface temperature with the highest fluxes being released at the sub-solar point where surface temperatures can reach 165 K and the lowest fluxes being released on Callisto's night-side with temperatures as low as 80 K (Moore et al., 2004). Sublimation is constrained by Callisto's water ice surface where most species are sublimated away together with the H_2O molecules. In contrast to Earth's Moon, where the ions inducing sputtering originate in the solar wind, Callisto is most of the time shielded from the solar wind by Jupiter's magnetosphere. However, the ions contained in Jupiter's magnetosphere act as sputtering agents. These ions consist mainly of O^{n+}, S^{n+}, and H^+ with ion fluxes of $\sim 1.92 \cdot 10^{10}\ \mathrm{m}^{-2}\ \mathrm{s}^{-1}$ and speeds of ~192 km/s (Kivelson et al., 2007). Photon stimulated desorption becomes less significant the further away an object is located from the Sun. While this process thus is not as significant at Callisto as, for example, at the Moon and Mercury, it does release particles with initial velocities higher than thermal release (Wurz and Lammer, 2003). Desorption fluxes are thus low but persist up to elevated altitudes.

Exospheric loss processes include (1) gravitational escape, (2) ionization, and (3) surface adsorption. The escape velocity $v_{\mathrm{esc}} = 2441\ \mathrm{m\ s}^{-1}$ from Callisto's surface is very similar to the escape velocity on the Moon. With such a low escape velocity, many of the exospheric particles (especially the light ones) are lost to space through gravitational escape. Photo-ionization, as photon-stimulated desorption, scales with an object's distance from the Sun. The photo-ionization rate at Callisto is therefore very small, with typical photo-ionization rates between $1 \times 10^{-8}\ \mathrm{s}^{-1}$ and $1 \times 10^{-10}\ \mathrm{s}^{-1}$ depending on species (Huebner et al., 1992). In addition, electrons from the magnetospheric plasma contribute to ionization. Shematovich et al. (2005) give values on the order of $10^{-6}\ \mathrm{s}^{-1}$ for Europa, which we adapt for Callisto using electron densities presented in Table 21.1 in Kivelson et al. (2007). The resulting electron ionization rates at Callisto are on the order of $10^{-9}\ \mathrm{s}^{-1}$. Particles that do not escape Callisto's gravity, that are not lost due to ionization and that are not fragmented during their flight path, return to Callisto's surface.

Assuming that Callisto's exosphere is surface-bound, the surface composition should directly reflect the exospheric composition, which will be measured by NIM/PEP on JUICE, as well as by JUICE-MAJIS, SWI, UVS, and RPWI. In the following we describe Callisto's surface composition, the plasma environment in which Callisto is situated, and information about the model implementation. The exospheric densities are calculated with a Monte-Carlo model that is based on an earlier model adapted to Callisto (Wurz and Lammer, 2003; Wurz et al., 2007, 2010). Again, it is noteworthy that our modeling approach assumes a collision-less exosphere starting at the surface, which might have to be revised in a follow-up study of this paper.

3.1. Callisto surface composition

Whereas it is well established that Callisto consists of both ice and non-ice components, it is unclear what exactly their compositions are and what the ratio between the ice and non-ice component is (though ratios between the ice and non-ice component of about 1:1 are generally accepted (Greeley et al., 2000; Kuskov and Kronrod, 2005)). We therefore model particle release from both an ice and a non-ice surface separately.

In the absence of firm observational data, we model the ice composition of Callisto from formation models depicting the composition of its building blocks. To do so, we consider two extreme formation scenarios for the satellite: namely the condensation of its building blocks in the protosolar nebula (Mousis and Gautier, 2004; Mousis et al., 2009) or in an initially warm and dense jovian sub-nebula (Prinn and Fegley, 1981, 1989). In the first case, Callisto's building blocks are expected to be the same as those that have been accreted by Jupiter during its formation. To derive such a composition, a reasonable assumption is to use the planetesimal composition model of Mousis et al. (2012), where the condensation of the different ices in the protosolar nebula is computed from the use of equilibrium curves of hydrates, clathrates and pure condensates as well as the thermodynamic path detailing the evolution of temperature and pressure at the current location of Jupiter in the protosolar nebula. The model of Mousis et al. (2012) is based on a predefined initial gas phase composition in which all elemental abundances reflect the bulk abundances of the Sun. Oxygen, carbon, nitrogen, sulfur and phosphorus are postulated to exist only in the forms of H_2O, CO, CO_2, CH_3OH, CH_4, N_2, NH_3, H_2S, and PH_3. Gas phase conditions in the protosolar nebula are considered oxidizing, implying that most of C is in CO and most of N is in N_2 (Johnson et al., 2012). Therefore, we assumed that $CO:CO_2:CH_3OH:CH_4 = 70:10:2:1$ and $N_2:NH_3 = 10$ in the gas phase of the disk, a set of values consistent with interstellar medium measurements (Mousis et al., 2012). In the second case, Callisto's building blocks are expected to condense in reducing conditions in the jovian sub-nebula, implying that essentially all C and N were in the forms of CH_4 and NH_3 in this environment, respectively (Prinn and Fegley, 1981, 1989). In this case, we assume that ices condensed from a gas phase where all C is in CH_4 and $N_2:NH_3 = 0.1$. In both extreme cases, sulfur is assumed to exist in the form of H_2S, with an abundance fixed to half its protosolar value, and other refractory sulfide components (Pasek et al., 2005). Finally, in both cases, we added Na and K species to the composition in the water ice, both of which we assumed to have a mole fraction of about 10^{-3} of the H_2O mole fraction assuming the water ice on the surface is similar to the salty ocean under the surface (Zimmer et al., 2000). Table 1 lists the mole fractions of the most common species for the oxidizing and reducing states.

Callisto's low albedo and existence of other non-ice features imply that at least part of the surface consists of a non-ice mineral (Showman and Malhotra, 1999). According to Calvin et al. (1995), who presented a compilation of visible to near-infrared data of the Galilean satellites' surfaces, the Callisto spectra are the least suggestive of water ice. The non-ice component exhibits spectral properties from 0.2 to 4 μm that are similar to those of phyllosilicate minerals commonly found in carbonaceous chondrite meteorites (Calvin and Clark, 1991). On the other hand Kuskov and Kronrod (2001) state that objects having condensed at large distance from Jupiter (like Europa, Ganymede, and Callisto) must not consist of C chondritic materials, because these materials have too large Fe/Si ratios. Instead, they propose that the non-ice material on Callisto's surface is similar to the material contained in L and LL chondrites. We implemented both compositions of CI and L chondrites for the non-ice material in our study, and present their most important mole fractions in Table 2 with values taken from Wasson and Kallemeyn (1988).

Table 1
Callisto's ice composition: Mole fractions of the most common species of the oxidizing and reducing initial gas phase conditions in the solar nebula.

Species	Mole fraction	
	Oxidizing	Reducing
H_2O	0.598	0.730
CO	0.261	0
CO_2	0.068	0
CH_3OH	0.016	0
CH_4	0.006	0.197
N_2	0.027	0.002
NH_3	0.007	0.062
H_2S	0.014	0.007
PH_3	2.05×10^{-4}	2.49×10^{-4}
Ar	0.002	0.001
Kr	2.05×10^{-6}	9.79×10^{-7}
Xe	3.20×10^{-7}	1.15×10^{-7}
Na	5.98×10^{-4}	7.30×10^{-4}
K	5.98×10^{-4}	7.30×10^{-4}
Sum	1	1

Table 2
Callisto's non-ice composition: Mole fractions of the most common species in CI and L type chondrites.

Species	Mole fraction	
	CI type chondrites	L type chondrites
O	0.440	0.556
H	0.304	0
Si	0.057	0.155
Mg	0.061	0.145
Fe	0.050	0.091
S	0.028	0.016
Al	0.005	0.011
Ca	0.004	0.008
Na	0.003	0.007
Ni	0.003	0.005
C	0.041	0.002
Cr	7.80×10^{-4}	0.002
Mn	5.29×10^{-4}	0.001
P	5.04×10^{-4}	7.23×10^{-4}
K	2.27×10^{-4}	4.98×10^{-4}
Ti	1.34×10^{-4}	3.10×10^{-4}
Co	1.32×10^{-4}	2.36×10^{-4}
N	0.002	0.72×10^{-4}
Sum	1	1

3.2. Jovian plasma environment

Since Callisto is well located inside Jupiter's magnetosphere, it interacts primarily with Jupiter's co-rotating magnetospheric plasma rather than directly with the solar wind. The relevant plasma parameters that are required to simulate particle release from a surface due to ion sputtering are (1) the plasma composition, (2) the plasma velocity, and (3) and the plasma flux.

According to Cooper et al. (2001), Frank et al. (2002), Kivelson et al. (2007), Bagenal (2004), the most common species in Jupiter's magnetospheric plasma are H, O and S ions. Their relative abundance is not well known and changes with distance from Jupiter (Bagenal et al., 1992). We assume values of 0.1:0.18:0.72 for the H:O:S ion abundances. Jupiter's magnetospheric plasma is known to approximately co-rotate with Jupiter. Table 21.2 in Kivelson et al. (2007) lists the azimuthal velocity of the plasma at the different Galilean satellites' locations, with a mean value of 200 km/s and a range from 130 to 280 km/s at Callisto's radial distance. The Galilean satellites themselves orbit Jupiter in the same direction as the plasma, but at much smaller velocities. The jovian plasma therefore flows over the satellites from their trailing hemispheres with a relative speed equal to the local co-rotation speed minus the satellites' orbital speeds. Callisto's average orbital speed is 8.204 km/s, yielding a mean relative plasma velocity of 192 km/s as seen from Callisto. The total magnetospheric plasma density at Callisto's orbit is on average $\sim$0.1 cm^{-3}, with minimum and maximum values of 0.01 cm^{-3} and 0.5 cm^{-3}, respectively (Kivelson et al., 2007). The plasma flux impinging onto Callisto's surface can finally be computed for each species as the product between the plasma speed and the plasma density. Table 3 lists all jovian plasma parameters relevant for modeling sputtering from Callisto's surface.

3.2.1. Mineral sputter yields

From the chemical composition of Callisto's non-ice surface and the relevant parameters of the plasma interacting with Callisto's surface, we determine the sputter yields for each species present on the surface for each ion population present in the plasma. The sputter yield is the average number of atoms sputtered from the surface for an impinging ion. To determine the sputter yields we used the Stopping and Range of Ions in Matter (SRIM) tool-suite, which calculates ion interactions with matter (http://www.srim.org). SRIM applies a Monte-Carlo simulation method to calculate

Table 3
Jovian plasma environment at Callisto. Given, where applicable, are the mean values and the minimal and maximal values in parentheses.

Species	Mass (amu)	Speed (km/s)	Ion density (cm^{-3})	Ion flux (s^{-1} m^{-2})
H	1.008	192 (122–272)	0.010 (0.001–0.050)	1.92 e9 (1.92 e8–9.60 e9)
O	15.995	192 (122–272)	0.072 (0.007–0.360)	1.38 e10 (1.38 e9–6.90 e10)
S	31.972	192 (122–272)	0.018 (0.002–0.090)	3.46 e9 (3.46 e8–1.73 e10)

the binary collision between an ion and a surface of a given chemical composition. Input parameters for the ion are the ion's mass, the ion's energy, and the angle of incidence. Input parameters for the surface are the present atoms' weight percentages, the thickness of the simulated layer and the layer's density. The masses and velocities of the impinging ions (H, O, and S) are presented in Table 3, and the angle of incidence was taken to be 45°. The sputter yield for a smooth surface is a strong function of incidence angle, but for a rough surface, typical for a planetary surface, the angle of incidence dependence averages out and the sputter yields have about the same value as for a smooth surface at 45° impact (Küstner et al., 1998; Wurz et al., 2007). The species present in the non-ice material and their weight percentages are presented in Table 2. A quick simulation showed that a thickness of 10,000 Å was more than sufficient for the given ion energy (i.e., the impinging ions only slightly penetrated into the material). The layer's density was chosen to be 3.5 g/cm^3, which is in good agreement with values presented by Nagel et al. (2004) and Kuskov and Kronrod (2005). For each surface species, plasma species and plasma velocity we ran 100,000 simulations. Tables 4 and 5 list the sputter yields for non-ice sputtering by H, O, and S at five different velocities for the two non-ice materials.

3.2.2. Ice sputter yields

Sputtering of water ice is not only a nuclear interaction process, like ion sputtering of minerals, but mostly involves electronic excitations, which results in much higher sputter yields. For example, for solar wind protons the sputter yield of water ice is about a factor 10 higher than for sputtering of mineral grains (Shi et al., 1995), with a sputter yield of ≈0.7 water molecules per proton. For heavier ions the sputter yields is even larger, as well as for higher energies. At lower energies these sputter yields have been extrapolated to lower energies on the basis of the nuclear stopping power. Recently, measurements have been performed in the lower energy range (Famá et al., 2008; Galli et al., submitted for publication) and the correlation of the sputter yield with nuclear stopping power has been demonstrated. Famá et al. (2008) also found a temperature dependence of the sputter yield

$$Y^{SP}_{H_2O} = Y_0 + Y_1 \exp\left(-\frac{E_{SP}}{k_B T}\right) \tag{1}$$

where Y_0 is the sputter yield below 80 K, Y_1 the prefactor for the temperature dependent sputter yield, E_{SP} the activation energy of 0.06 eV, k_B the Boltzmann constant, and T is the absolute temperature. We implemented the sputter yields presented in Cassidy et al. (2010) and used the formalism given by Famá et al. (2008) for low ion energies. Since the ice sputter yields depend on the surface temperature, we present sputter yields for the sub-solar point as well as the night-side. Tables 6 and 7 list the computed yields for ice sputtering by H, O, and S at five different velocities for the two ice materials.

3.3. Implementation

The Monte-Carlo model used to compute the particle densities in the exosphere presented herein is an updated version of the model presented in Wurz and Lammer (2003) and Wurz et al. (2007). In this model the trajectories of a certain amount of particles (henceforth called loop size) are simulated one by one from their point of origin (the surface), until the particle either (1) leaves Callisto's gravity field, (2) has returned to the surface, (3) has been ionized, or, in case of a molecule, (4) has been fragmented. If a molecule is fragmented, its current velocity plus a fraction of the dissociation energy released during the particle's break up is used to compute the fragments' initial velocities, which are modeled until they themselves reach a stop criterion.

The particles' initial velocities are computed according to the equations given in Wurz and Lammer (2003) and Wurz et al. (2007). For convenience, we restate the theoretical sublimation, sputter and photon stimulated desorption velocity equations here:

$$v_{\text{therm}} = \sqrt{\frac{8k_B T_0}{\pi m}}, \tag{2}$$

$$v_{\text{sputt}} = \frac{1}{2} v_1^2 v_2 \left(-\frac{3v_1^2 + 5v_2^2}{v_1^2 + v_2^2} + \frac{3\arctan(v_2/v_1)}{v_1 v_2}\right), \tag{3}$$

$$v_{\text{psd}} = \frac{3}{4}\sqrt{\frac{2\pi T_0 k_B}{m}} \frac{\Gamma(\beta - 0.5)}{\Gamma(\beta)}, \tag{4}$$

with the abbreviations $v_1 = \sqrt{\frac{2E_{b,i}}{m}}$ and $v_2 = \frac{4v_{\text{ion}}}{m+m_{\text{ion}}}$, where k_B is the Boltzmann constant, T_0 is the surface temperature, m is the mass of the particle that is released, $E_{b,i}$ is the binding energy of species i in the particular chemical mix of the surface, v_{ion} and m_{ion} are the velocity and the mass of the incoming ion, respectively, where Γ is the gamma function and where β the shape parameter of the distribution. β was chosen to be equal to 0.7, which is the value Johnson et al. (2002) gives for Na at Europa.

In the Monte-Carlo model each particle is assigned an initial velocity equal to the product of the theoretical velocity and a Gauss derivative (c.f. Wurz and Lammer (2003)). The particle's initial velocity is split up into a radial and a tangential component according to the particle's release angle, which is taken from a uniform distribution over 2π (see Wurz and Lammer (2003), Wurz et al. (2007)). Once a particle's initial velocity components have been determined, its Keplerian trajectory is computed by an 8th order f- and g-Series algorithm as described in Schaufelberger et al. (2011). Having simulated all particles' trajectories, we can compute the species' density profiles by multiplying the species' surface densities with the fraction of particles present at a certain altitude. The surface densities of the different species are presented in the following for the different release processes.

3.3.1. Sublimation of H_2O and main ice constituents

The surface density for water being released from the ice surface by sublimation can be computed according to the following equation:

$$N_0 = \frac{P_{\text{subl}}(T_0)}{k_B T_0}, \tag{5}$$

where $P_{\text{subl}}(T)$ is the water vapor pressure, k_B the Boltzmann constant, and where T_0 is the surface temperature. We compute the water vapor pressure from Eqs. (5) and (6) in Fray and Schmitt (2009), which we restate here for convenience:

$$\ln\left(\frac{P_{\text{subl}}(T)}{P_t}\right) = \frac{3}{2}\ln\left(\frac{T}{T_t}\right) + \left(1 - \frac{T_t}{T}\right)\eta\left(\frac{T}{T_t}\right) \tag{6}$$

$$\eta\left(\frac{T}{T_t}\right) = \sum_{i=0}^{6} e_i \left(\frac{T}{T_t}\right)^i, \tag{7}$$

where T_t and P_t stand for the temperature and pressure at the triple point, respectively, and where e_i are the coefficients given by the semi-empirical relation for the sublimation pressure of crystalline Ih water ice. Both triple point values and the six coefficients are given by Tables 2 and 6 in Fray and Schmitt (2009). Since the ice surface does not consist of pure water ice, this surface density has to be multiplied with the H_2O surface mole fraction, which is given in Table 1 for the oxidizing and the reducing case.

The sublimation dynamics for all other species in the water ice mixture are dominated by the water ice sublimation. We therefore compute the surface densities of all other main ice constituents

Table 4
Sputter yields for a non-ice material resembling CI chondrites.

	120 km/s			160 km/s			200 km/s			240 km/s			280 km/s		
	H	O	S	H	O	S	H	O	S	H	O	S	H	O	S
O	0.00000	0.18900	3.27000	0.01630	2.30000	3.82000	0.03990	2.44000	4.13000	0.05200	2.46000	4.30000	0.05500	2.45000	4.35000
H	0.00000	0.76100	1.23000	0.03090	0.91980	1.52000	0.03730	1.02000	1.71000	0.03780	1.05000	1.83000	0.03750	1.07000	1.91000
Si	0.00000	0.14950	0.25050	0.00067	0.17650	0.29810	0.00238	0.18990	0.32450	0.00331	0.19250	0.34220	0.00365	0.19650	0.34620
Mg	0.00000	0.33910	0.54700	0.00282	0.39310	0.64690	0.00709	0.41270	0.69380	0.00915	0.41630	0.72580	0.00929	0.41440	0.73060
Fe	0.00000	0.13270	0.23020	0.00025	0.15990	0.27650	0.00165	0.17440	0.30590	0.00239	0.17860	0.32010	0.00248	0.17900	0.32730
S	0.00000	0.10370	0.17610	0.00035	0.12340	0.21220	0.00143	0.13330	0.22360	0.00217	0.13440	0.23840	0.00253	0.13490	0.24110
Al	0.00000	0.01470	0.02410	0.00007	0.01810	0.03070	0.00022	0.01980	0.03300	0.00040	0.01980	0.03480	0.00042	0.01970	0.03480
Ca	0.00000	0.01860	0.03180	0.00005	0.02210	0.03700	0.00025	0.02390	0.03990	0.00039	0.02330	0.04100	0.00055	0.02320	0.04210
Na	0.00000	0.02200	0.03550	0.00025	0.02560	0.04140	0.00042	0.02680	0.04480	0.00065	0.02680	0.04550	0.00062	0.02610	0.04730
Ni	0.00000	0.00710	0.01350	0.00000	0.00902	0.01410	0.00004	0.00979	0.01650	0.00008	0.00949	0.01800	0.00014	0.00950	0.01820
C	0.00000	0.06310	0.10730	0.00020	0.07590	0.13100	0.00115	0.08360	0.14560	0.00131	0.08660	0.15780	0.00134	0.08650	0.16200
Cr	0.00000	0.00221	0.00387	0.00000	0.00271	0.00459	0.00004	0.00265	0.00516	0.00004	0.00309	0.00511	0.00007	0.00293	0.00520
Mn	0.00000	0.00208	0.00326	0.00001	0.00256	0.00430	0.00004	0.00256	0.00403	0.00005	0.00228	0.00468	0.00004	0.00252	0.00450
P	0.00000	0.00174	0.00281	0.00000	0.00217	0.00332	0.00005	0.00198	0.00371	0.00005	0.00227	0.00357	0.00002	0.00247	0.00433
K	0.00000	0.00211	0.00306	0.00002	0.00191	0.00324	0.00002	0.00201	0.00343	0.00008	0.00197	0.00391	0.00007	0.00211	0.00358
Ti	0.00000	0.00035	0.00058	0.00000	0.00041	0.00062	0.00001	0.00039	0.00079	0.00000	0.00052	0.00074	0.00000	0.00040	0.00079
Co	0.00000	0.00035	0.00066	0.00000	0.00048	0.00054	0.00000	0.00036	0.00092	0.00000	0.00057	0.00088	0.00002	0.00038	0.00091
N	0.00000	0.00775	0.01220	0.00006	0.00883	0.01460	0.00019	0.00877	0.01510	0.00018	0.00881	0.01570	0.00011	0.00899	0.01540

Table 5
Sputter yields for a non-ice material resembling L chondrites.

	120 km/s			160 km/s			200 km/s			240 km/s			280 km/s		
	H	O	S	H	O	S	H	O	S	H	O	S	H	O	S
O	0.00000	2.41000	3.95000	0.00185	2.76000	4.60000	0.02640	2.91000	4.92000	0.04340	2.93000	5.09000	0.05210	2.92000	5.18000
Si	0.00000	0.38640	0.63530	0.00051	0.45140	0.76390	0.00412	0.48600	0.83130	0.00563	0.49440	0.86750	0.00662	0.49970	0.89590
Mg	0.00000	0.77810	1.27000	0.00043	0.88800	1.47000	0.00854	0.93080	1.58000	0.01350	0.93790	1.61000	0.01720	0.93370	1.64000
Fe	0.00000	0.24150	0.40820	0.00021	0.28570	0.48840	0.00200	0.30990	0.53700	0.00318	0.31620	0.55880	0.00386	0.31740	0.57670
S	0.00000	0.06070	0.09980	0.00004	0.07070	0.11600	0.00048	0.07540	0.12770	0.00113	0.07540	0.13190	0.00131	0.07480	0.13550
Al	0.00000	0.03220	0.05400	0.00000	0.03630	0.06180	0.00034	0.03950	0.06710	0.00054	0.03910	0.07010	0.00058	0.03950	0.07110
Ca	0.00000	0.04320	0.06910	0.00005	0.04740	0.07960	0.00036	0.05020	0.08560	0.00071	0.05190	0.08920	0.00080	0.05180	0.09190
Na	0.00000	0.04590	0.07900	0.00004	0.05310	0.08660	0.00052	0.05770	0.09540	0.00076	0.05650	0.09780	0.00119	0.05600	0.09900
Ni	0.00000	0.01310	0.02070	0.00001	0.01430	0.02680	0.00018	0.01650	0.02880	0.00012	0.01670	0.02920	0.00020	0.01660	0.03000
C	0.00000	0.00249	0.00453	0.00000	0.00310	0.00495	0.00002	0.00341	0.00531	0.00002	0.00364	0.00557	0.00003	0.00340	0.00611
Cr	0.00000	0.00536	0.00822	0.00001	0.00547	0.01010	0.00002	0.00636	0.01030	0.00008	0.00606	0.01120	0.00006	0.00610	0.01190
Mn	0.00000	0.00380	0.00650	0.00002	0.00455	0.00785	0.00002	0.00506	0.00865	0.00005	0.00514	0.00915	0.00002	0.00509	0.00904
P	0.00000	0.00209	0.00429	0.00000	0.00270	0.00509	0.00004	0.00262	0.00516	0.00005	0.00329	0.00510	0.00004	0.00304	0.00531
K	0.00000	0.00382	0.00700	0.00002	0.00446	0.00773	0.00003	0.00497	0.00819	0.00010	0.00486	0.00793	0.00002	0.00487	0.00861
Ti	0.00000	0.00083	0.00136	0.00000	0.00095	0.00129	0.00000	0.00105	0.00171	0.00000	0.00081	0.00171	0.00000	0.00094	0.00164
Co	0.00000	0.00067	0.00125	0.00000	0.00070	0.00142	0.00000	0.00086	0.00143	0.00001	0.00080	0.00152	0.00000	0.00076	0.00149
N	0.00000	0.00019	0.00049	0.00000	0.00023	0.00053	0.00000	0.00029	0.00071	0.00002	0.00038	0.00044	0.00000	0.00033	0.00060

based on their sublimation fluxes, which are expected to be equal to the H_2O sublimation flux multiplied with the mole fraction of the species to the H_2O mole fraction.

3.3.2. Sublimation of H, O, OH, H_2, O_2, and O_3

We also implement sublimation of the H_2O radiolysis products, i.e., H, O, and OH. The flux ratio of these fragments with respect to H_2O was taken to be 0.055. This is the ratio that Marconi (2007) gives for H, O and OH to H_2O on Ganymede.

Finally, we implemented thermal release of H_2, O_2, and O_3, which are also radiolysis products of H_2O, but which have undergone recombination and which stay more or less stable in the exosphere. The Callisto O_2 surface density was taken from Kliore et al. (2002), who had computed the neutral O_2 surface density required to reproduce the ionosphere measurements conducted by the Galileo mission. They obtained an average surface density value of $(1.78 \pm 0.24) \times 10^{10}$ cm^{-3} for a solar zenith angle of $\sim 81°$. We assume that the O_2 column density is the same on Callisto's complete surface since O_2 is not expected to condense on the night-side, and adjust the surface density accordingly for other solar zenith angles and night side. Since we do not have any measurements of the surface densities of H_2 and O_3, we estimated their exospheric densities at the surface to be at $N_0 = 1.2 \times 10^6$ cm^{-3} and $N_0 = 1.4 \times 10^2$ cm^{-3}, respectively. This estimate takes into account the recombination of the radiolysis products to form H_2 and O_3, and their survival in Callisto's exosphere.

3.3.3. Sputtering of ice constituents

The surface density of each sputtered ice constituent is equal to the flux released from the ice surface divided by the particle velocity. The flux released from the surface is equal to the product of the flux of impinging ions (presented in Table 3) and the species' sputter yield. The sputter yields were interpolated from the values presented in Tables 6 and 7, which give sputter yields for the sub-solar point and the night-side, for ion velocities as listed in Table 3. The particle velocity was computed according to Eq. (3).

3.3.4. Sputtering of non-ice constituents

Computing the surface densities of particles sputtered from the non-ice material (mineral sputtering) is similar to computing particles being sputtered from the ice material. In addition, though, one also has to take the surface porosity into account, since it linearly scales the sputter yield (c.f. Wurz et al. (2007)). As Wurz et al.

Table 6
Sputter yields for species being sputtered from the sub-solar point (top) and night-side (bottom) of the oxidizing state ice composition.

	120 km/s			160 km/s			200 km/s			240 km/s			280 km/s		
	H	O	S	H	O	S	H	O	S	H	O	S	H	O	S
H_2O	1.30E−02	1.73E−03	1.24E−03	1.97E−02	2.65E−03	1.91E−03	2.70E−02	3.70E−03	2.67E−03	3.49E−02	4.84E−03	3.51E−03	4.33E−02	6.07E−03	4.41E−03
CO	5.67E−03	7.53E−04	5.40E−04	8.58E−03	1.16E−03	0.00E+00	1.18E−02	1.61E−03	1.17E−03	1.52E−02	2.11E−03	1.53E−03	1.89E−02	2.65E−03	1.93E−03
CO_2	1.49E−03	1.98E−04	1.42E−04	2.25E−03	3.04E−04	0.00E+00	3.09E−03	4.23E−04	3.06E−04	4.00E−03	5.54E−04	4.02E−04	4.96E−03	6.95E−04	5.05E−04
CH_3OH	3.51E−04	4.66E−05	3.34E−05	5.31E−04	7.17E−05	0.00E+00	7.29E−04	9.98E−05	7.22E−05	9.43E−04	1.31E−04	9.48E−05	1.17E−03	1.64E−04	1.19E−04
CH_4	1.25E−04	1.65E−05	1.19E−05	1.89E−04	2.54E−05	5.14E−04	2.59E−04	3.54E−05	2.56E−05	3.35E−04	4.64E−05	3.36E−05	4.15E−04	5.82E−05	4.23E−05
N_2	5.92E−04	7.85E−05	5.64E−05	8.95E−04	1.21E−04	5.61E−06	1.23E−03	1.68E−04	1.22E−04	1.59E−03	2.20E−04	1.60E−04	1.97E−03	2.76E−04	2.01E−04
NH_3	1.53E−04	2.03E−05	1.46E−05	2.31E−04	3.12E−05	1.61E−04	3.18E−04	4.35E−05	3.15E−05	4.11E−04	5.70E−05	4.13E−05	5.09E−04	7.14E−05	5.19E−05
H_2S	3.15E−04	4.17E−05	3.00E−05	4.76E−04	6.42E−05	1.81E−05	6.53E−04	8.94E−05	6.47E−05	8.45E−04	1.17E−04	8.49E−05	1.05E−03	1.47E−04	1.07E−04
PH_3	1.13E−05	1.50E−06	1.08E−06	1.71E−05	2.31E−06	6.51E−07	2.35E−05	3.22E−06	2.33E−06	3.04E−05	4.22E−06	3.06E−06	3.77E−05	5.29E−06	3.85E−06
Ar	4.62E−05	6.13E−06	4.40E−06	6.99E−05	9.43E−06	2.66E−06	9.60E−05	1.31E−05	9.50E−06	1.24E−04	1.72E−05	1.25E−05	1.54E−04	2.16E−05	1.57E−05
Kr	4.46E−08	5.92E−09	4.25E−09	6.74E−08	9.10E−09	2.57E−09	9.26E−08	1.27E−08	9.17E−09	1.20E−07	1.66E−08	1.20E−08	1.48E−07	2.08E−08	1.51E−08
Xe	6.96E−09	9.24E−10	6.63E−10	1.05E−08	1.42E−09	3.01E−10	1.45E−08	1.98E−09	1.43E−09	1.87E−08	2.59E−09	1.88E−09	2.32E−08	3.25E−09	2.36E−09
H_2O	3.18E−03	4.22E−04	3.03E−04	4.81E−03	6.50E−04	4.68E−04	6.61E−03	9.05E−04	6.54E−04	8.54E−03	1.18E−03	8.59E−04	1.06E−02	1.49E−03	1.08E−03
CO	1.39E−03	1.84E−04	1.32E−04	2.10E−03	2.83E−04	2.04E−04	2.88E−03	3.95E−04	0.00E+00	3.73E−03	5.17E−04	3.75E−04	4.62E−03	6.48E−04	4.71E−04
CO_2	3.64E−04	4.84E−05	3.47E−05	5.51E−04	7.44E−05	5.36E−05	7.57E−04	1.04E−04	0.00E+00	9.79E−04	1.36E−04	9.84E−05	1.21E−03	1.70E−04	1.24E−04
CH_3OH	8.59E−05	1.14E−05	8.19E−06	1.30E−04	1.75E−05	1.26E−05	1.79E−04	2.44E−05	0.00E+00	2.31E−04	3.20E−05	2.32E−05	2.86E−04	4.01E−05	2.92E−05
CH_4	3.05E−05	4.05E−06	2.91E−06	4.61E−05	6.23E−06	4.49E−06	6.34E−05	8.67E−06	1.76E−04	8.19E−05	1.14E−05	8.23E−06	1.02E−04	1.42E−05	1.04E−05
N_2	1.45E−04	1.92E−05	1.38E−05	2.19E−04	2.96E−05	2.13E−05	3.01E−04	4.12E−05	1.92E−06	3.89E−04	5.39E−05	3.91E−05	4.82E−04	6.76E−05	4.92E−05
NH_3	3.75E−05	4.97E−06	3.57E−06	5.67E−05	7.65E−06	5.51E−06	7.78E−05	1.07E−05	5.52E−05	1.01E−04	1.39E−05	1.01E−05	1.25E−04	1.75E−05	1.27E−05
H_2S	7.70E−05	1.02E−05	7.33E−06	1.16E−04	1.57E−05	1.13E−05	1.60E−04	2.19E−05	6.19E−06	2.07E−04	2.87E−05	2.08E−05	2.56E−04	3.59E−05	2.61E−05
PH_3	2.77E−06	3.68E−07	2.64E−07	4.20E−06	5.66E−07	4.08E−07	5.76E−06	7.89E−07	2.23E−07	7.45E−06	1.03E−06	7.49E−07	9.24E−06	1.30E−06	9.42E−07
Ar	1.13E−05	1.50E−06	1.08E−06	1.71E−05	2.31E−06	1.66E−06	2.35E−05	3.22E−06	9.09E−07	3.04E−05	4.21E−06	3.05E−06	3.77E−05	5.28E−06	3.84E−06
Kr	1.09E−08	1.45E−09	1.04E−09	1.65E−08	2.23E−09	1.61E−09	2.27E−08	3.10E−09	8.78E−10	2.93E−08	4.06E−09	2.95E−09	3.63E−08	5.09E−09	3.71E−09
Xe	1.70E−09	2.26E−10	1.62E−10	2.58E−09	3.48E−10	2.51E−10	3.54E−09	4.85E−10	1.03E−10	4.58E−09	6.34E−10	4.60E−10	5.67E−09	7.95E−10	5.78E−10

Table 7
Sputter yields for species being sputtered from the sub-solar point (top) and night-side (bottom) of the reducing state ice composition.

	120 km/s			160 km/s			200 km/s			240 km/s			280 km/s		
	H	O	S	H	O	S	H	O	S	H	O	S	H	O	S
H_2O	1.59E−02	2.11E−03	1.52E−03	2.41E−02	3.25E−03	2.34E−03	3.30E−02	4.52E−03	3.27E−03	4.27E−02	5.92E−03	4.29E−03	5.30E−02	7.42E−03	5.40E−03
CH_4	4.28E−03	5.68E−04	4.08E−04	6.47E−03	8.73E−04	6.29E−04	8.89E−03	1.22E−03	8.80E−04	1.15E−02	1.59E−03	1.16E−03	1.43E−02	2.00E−03	1.45E−03
N_2	4.67E−05	6.20E−06	4.45E−06	7.06E−05	9.53E−06	6.87E−06	9.70E−05	1.33E−05	9.60E−06	1.25E−04	1.74E−05	1.26E−05	1.56E−04	2.18E−05	1.59E−05
NH_3	1.34E−03	1.78E−04	1.28E−04	2.03E−03	2.74E−04	1.97E−04	2.79E−03	3.81E−04	2.76E−04	3.60E−03	4.99E−04	3.62E−04	4.46E−03	6.26E−04	4.55E−04
H_2S	1.50E−04	2.00E−05	1.43E−05	2.28E−04	3.07E−05	2.21E−05	3.13E−04	4.28E−05	3.09E−05	4.04E−04	5.60E−05	4.06E−05	5.01E−04	7.02E−05	5.11E−05
PH_3	5.42E−06	7.19E−07	5.16E−07	8.19E−06	1.11E−06	7.97E−07	1.13E−05	1.54E−06	1.11E−06	1.45E−05	2.02E−06	1.46E−06	1.80E−05	2.53E−06	1.84E−06
Ar	2.21E−05	2.93E−06	2.11E−06	3.34E−05	4.51E−06	3.25E−06	4.59E−05	6.28E−06	4.54E−06	5.93E−05	8.22E−06	5.97E−06	7.36E−05	1.03E−05	7.50E−06
Kr	2.13E−08	2.83E−09	2.03E−09	3.23E−08	4.36E−09	3.14E−09	4.43E−08	6.07E−09	4.39E−09	5.73E−08	7.94E−09	5.76E−09	7.10E−08	9.96E−09	7.24E−09
Xe	2.50E−09	3.32E−10	2.38E−10	3.78E−09	5.11E−10	3.68E−10	5.20E−09	7.11E−10	5.14E−10	6.72E−09	9.31E−10	6.75E−10	8.33E−09	1.17E−09	8.49E−10
H_2O	3.89E−03	5.17E−04	3.71E−04	5.89E−03	7.95E−04	5.73E−04	8.09E−03	1.11E−03	8.01E−04	1.05E−02	1.45E−03	1.05E−03	1.05E−03	1.82E−03	1.32E−03
CH_4	1.05E−03	1.39E−04	9.98E−05	1.58E−03	2.14E−04	1.54E−04	2.18E−03	2.98E−04	2.15E−04	2.81E−03	3.90E−04	2.83E−04	2.83E−04	4.89E−04	3.56E−04
N_2	1.14E−05	1.52E−06	1.09E−06	1.73E−05	2.33E−06	1.68E−06	2.38E−05	3.25E−06	2.35E−06	3.07E−05	4.25E−06	3.09E−06	3.09E−06	5.34E−06	3.88E−06
NH_3	3.28E−04	4.36E−05	3.13E−05	4.96E−04	6.70E−05	4.83E−05	6.82E−04	9.33E−05	6.75E−05	8.81E−04	1.22E−04	8.86E−05	8.86E−05	1.53E−04	1.11E−04
H_2S	3.68E−05	4.89E−06	3.51E−06	5.57E−05	7.52E−06	5.42E−06	7.65E−05	1.05E−05	7.57E−06	9.89E−05	1.37E−05	9.94E−06	9.95E−06	1.72E−05	1.25E−05
PH_3	1.33E−06	1.76E−07	1.26E−07	2.01E−06	2.71E−07	1.95E−07	2.75E−06	3.77E−07	2.73E−07	3.56E−06	4.93E−07	3.58E−07	3.58E−07	6.19E−07	4.50E−07
Ar	5.41E−06	7.18E−07	5.15E−07	8.18E−06	1.10E−06	7.96E−07	1.12E−05	1.54E−06	1.11E−06	1.45E−05	2.01E−06	1.46E−06	1.46E−06	2.52E−06	1.84E−06
Kr	5.22E−09	6.93E−10	4.97E−10	7.90E−09	1.07E−09	7.68E−10	1.09E−08	1.49E−09	1.07E−09	1.40E−08	1.94E−09	1.41E−09	1.41E−09	2.44E−09	1.77E−09
Xe	6.12E−10	8.13E−11	5.83E−11	9.26E−10	1.25E−10	9.01E−11	1.27E−09	1.74E−10	1.26E−10	1.64E−09	2.28E−10	1.65E−10	1.65E−10	2.86E−10	2.08E−10

(2007) in their lunar model, we use a porosity of 50%, which seems to be a good value for the porosity of the uppermost layer of a mature regolith surface. The surface densities of sputtered non-ice constituents can thus be computed as the product of the impinging ion flux, the species' sputter yields, and the surface porosity divided the species' initial velocities. Again, the species' initial velocities are given by Eq. (3).

3.3.5. Photon stimulated desorption of H_2O

Photon stimulated desorption was only implemented for H_2O, since the other species susceptible to PSD, Na and K, have low abundance on the surface. The exospheric density at the surface can be computed by dividing the PSD flux of H_2O by the average velocity of release. The theoretical velocity of particles released by photon stimulated desorption was presented in Eq. (4). The desorbed H_2O particle flux is equal to the flux of impinging UV photons, their desorption yield, and the area where photon stimulated desorption occurs, which was set equal to 0.33.

The flux of impinging UV photons can be derived from the UV flux at 1 AU (Jursa, 1985; Wurz and Lammer, 2003), scaled to Callisto's orbit, which gives $\phi_{ph} = 1.19 \times 10^{14}$ ph. cm^{-2} s^{-1}, times the cosine of the angle of incidence. The H_2O desorption yield from a water ice film was measured by Westley et al. (1995) as function of surface temperature. They give a fit to their photon desorption yield measurements which we restate here for convenience:

$$Y(T) = Y_0 + Y_1 \exp(-E/k_B T), \tag{8}$$

where T is the temperature, k_B is the Boltzmann constant, Y_0 and Y_1 are fit parameters equal to 0.035 ± 0.002 and 0.13 ± 0.10, respectively, and where E is the activation energy, which Westley et al. (1995) state to be equal to $(29 \pm 6) \times 10^{-3}$ eV.

4. Results

In this section we present the exospheric density profiles for all species present in the ice and the non-ice surfaces. We computed 10^5 particles for each species, each release process, and each plasma composition. The sublimated species have scale heights much smaller than the sputtered species, i.e., their density profiles drop off much steeper. An initial simulation showed that the scale heights of sublimated species were on the order of several 100 km whereas the scale height of the sputtered species was on the order of several 1000 km. We therefore set the step size equal to 10 km for the sublimated species and to 100 km for the sputtered species. The maximum altitude was set to 10^5 km, which is about twice Callisto's Hill radius (i.e., the altitude at which particles' have escaped Callisto's gravitational attraction).

As mentioned above, the density profiles of sublimated species fall off much more rapidly with altitude than the density profiles of sputtered species. The density of water that has been sublimated from the day-side, for example, was shown to decrease by about 9 orders of magnitude in the given altitude interval. To have such a density curve resolved we would be required to run the simulation with at least 10^9 particles, which is not practical due to computational constraints. We therefore chose to extrapolate the sublimated density curves when the number of particles present at a certain altitude step has fallen bellow 10^{-4} of the initial number of particles. For the extrapolation we chose to fit a quadratic function, since this function resembles the density profiles at high altitudes. In addition, to get rid of local variations due to low statistics, we smoothed these profiles with a bin width of 10.

As mentioned in Section 3.3, we did not only compute the density profiles of the primary species' being released from Callisto's surface, but also from their fragments. In the following figures we only present the density profiles of the species as they are present on the surface (i.e., as listed in Tables 1 and 2). However, the presented density profiles include the density profiles of fragments if they match the original species (e.g., the curve for O includes the results for O sublimated directly from the surface, but also for O as a fragment of sublimated CO, CO_2, O_2, O_3 and OH).

Figs. 1 and 2 present the density profiles for particles that have been sublimated from Callisto's ice surface at the sub-solar point and from the night-side, respectively. They both show in two separate panels the results for the ice surface resembling the oxidizing (left) and reducing (right) state of the initial conditions in the sub-nebula. Note that not all species are present in both states, i.e., the reducing case contains no CO, CO_2 and CH_3OH.

Figs. 3 and 4 present the density profiles for particles that have been sputtered from Callisto's ice surface, again for the two ice compositions (left and right) at the sub-solar point and from the night-side. These density profiles show the sum of the particles sputtered by the magnetospheric H^+, O^{n+}, and S^{n+}. Again, as for the sublimated species, we only show the species as they are present in the ice material, but include fragments matching these species. Note that due to the much lower surface densities, the *y*-axes are different from the *y*-axes in Figs. 1 and 2. Also, due to the bigger step size, the *x*-axes of these plots start at 100 km rather than at 10 km.

Fig. 5 shows the density profiles for particles being released from the non-ice surface, with surface compositions resembling the compositions of CI chondrites (left) and L chondrites (right). Since sputtering of non-ice species is not temperature dependent, we only show one plot for non-ice sputtering. Again, the sputter curves show the sum of the particles being sputtered by the three magnetospheric ion components. The range of the axes in Fig. 5 is the same as for Figs. 3 and 4.

5. Discussion

5.1. Sublimation of ice constituents

The sublimated particles exhibit the highest surface densities. Their density curves fall off quickly with altitude, though, with only the light particles H and H_2 making an exception. Whereas thus most particles return to the surface, only H and H_2 show considerable escape fractions of ~65% and ~25%, respectively. The flatness of the density curves of H and H_2 in comparison to the other species is also reflected the species' scale heights, which is around 1000 km for H and H_2 and between 300 and 400 km for all other species. H_2 is the only species that is being directly ionized on more than a 1% level (at ~4%). Fragmentation in the exosphere only affects O_3 (~10%), H_2 (~5%), CH_4 (~2.5%) and OH (~1%). All other species have fragmentation rates smaller than 1%.

Due to the similarity of the fate of the particles of most species, the species are usually kept in order of their stoichiometric presence on the surface. The only noticeable exception are H and H_2 (which have much higher scale heights as discussed above) and O. The density curve of the O particles becomes increasingly shallower with altitude because fragments of other species are being added (mainly from O_3 and OH), about 70% of which have velocities higher than the escape velocity at the point of break-up due to the added dissociation energy.

On the night-side, only species that do not freeze out have significant density profiles. The curves of these species (H_2, Ar, Kr, Xe, N_2, CO, O_2, PH_3, CH_4 and O_3) are very similar to their sub-solar counterparts. We computed these density profiles assuming that the species have night-side column densities equal to the column

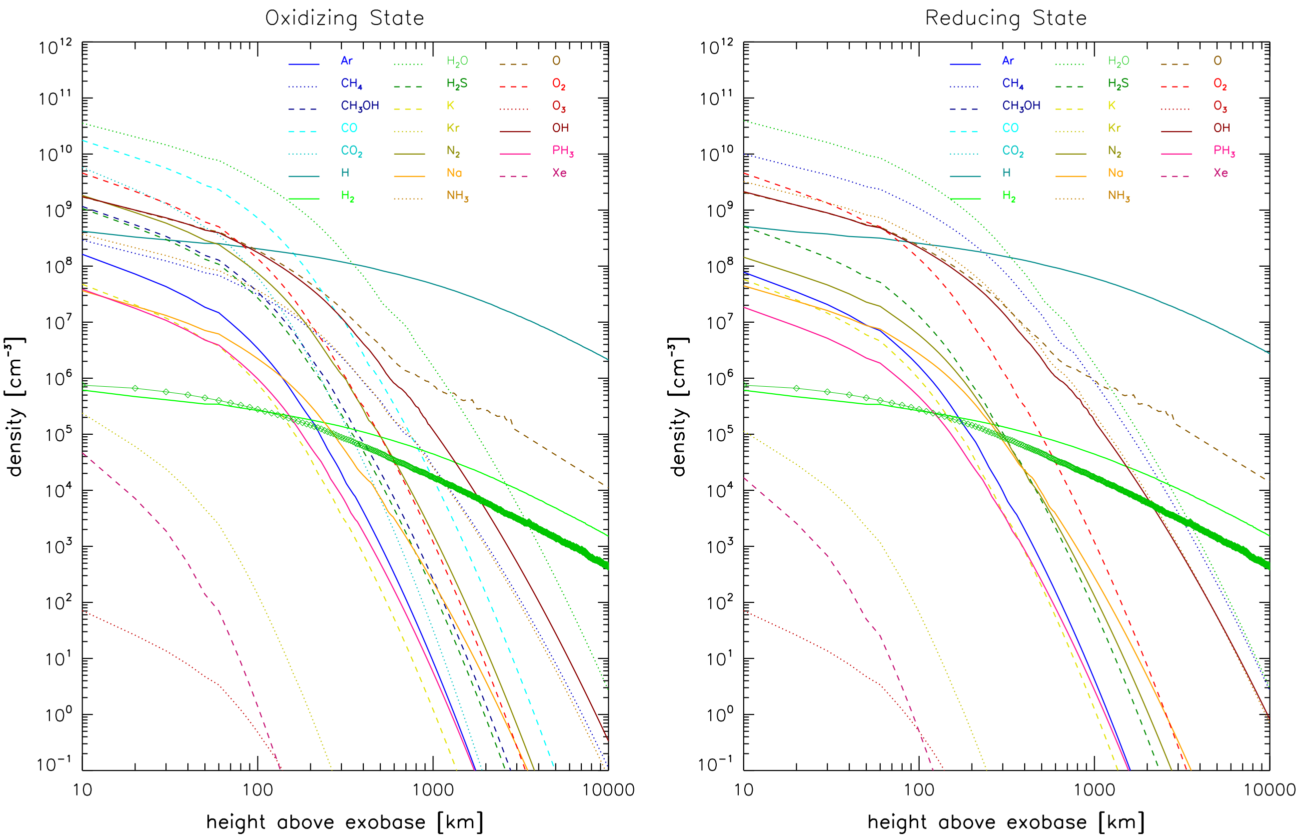

Fig. 1. Density profiles of particles that have been sublimated from Callisto's ice surface at the sub-solar point. The left panel shows the results for a surface composition resembling the oxidizing state of the sub-nebula and the right panel shows the results for the ice composition resembling the reducing state of the sub-nebula. Note that for H_2O two curves are shown: The curve with the diamonds shows photo desorbed H_2O.

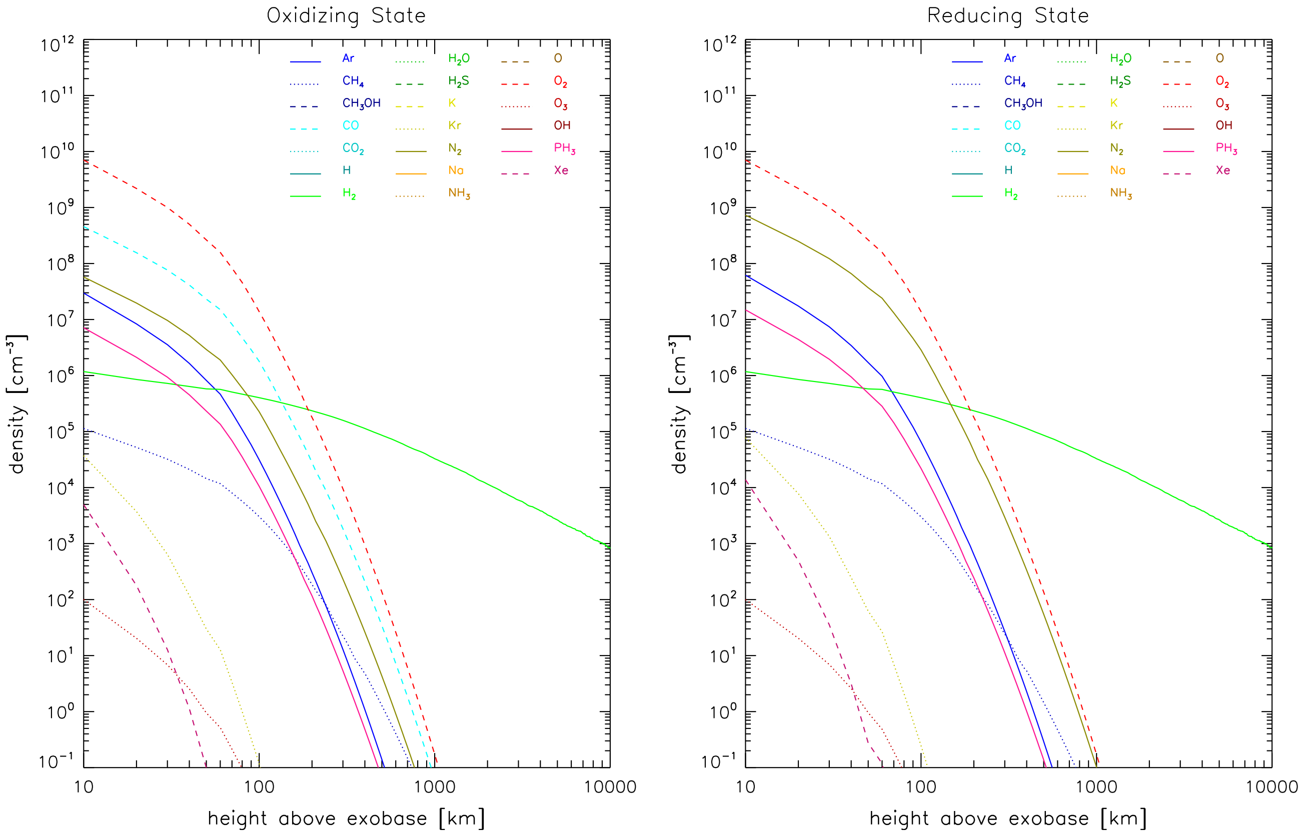

Fig. 2. Density profiles of particles that have been sublimated from Callisto's ice surface from the night side (sub-solar antipode). The left panel shows the results for a surface composition resembling the oxidizing state of the sub-nebula and the right panel shows the results for the ice composition resembling the reducing state of the sub-nebula. Note that for H_2O two curves are shown: The curve with the diamonds shows photo desorbed H_2O.

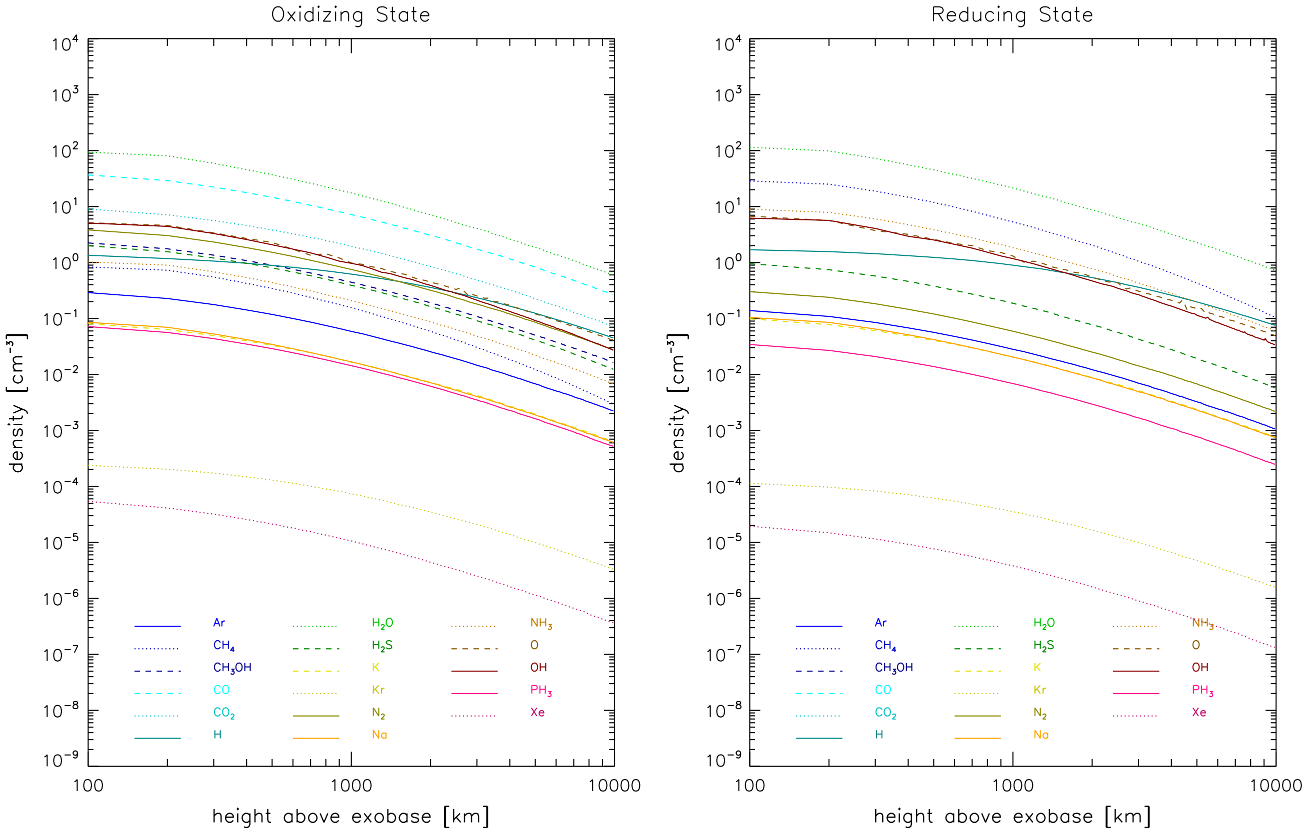

Fig. 3. Density profiles of particles that have been sputtered from Callisto's ice surface at the sub-solar point. The left panel shows the results for a surface composition resembling the oxidizing state of the sub-nebula and the right panel shows the results for the ice composition resembling the reducing state of the sub-nebula. The density profiles contain the results for sputtering by magnetospheric H^+, O^{n+}, and S^{n+}.

densities 30 deg from the sub-solar point, which we consider to be a good approximation.

Photon stimulated desorption of H_2O molecules produces surface particles with densities about 5 orders of magnitude smaller than sublimation, but with much higher release velocities (about 2 km/s compared to 440 m/s). Similarly to H and H_2, their density profiles are thus much shallower than the average sublimated species' density profile. No considerable part of desorbed H_2O is being ionized or fragmented, but about 7% of the particles are able to escape Callisto's Hill radius.

5.2. Sputtering of ice constituents

The density profiles of the sputtered species are quite different from the density profiles of the sublimated particles. On one hand, their density profiles start at much lower values than the density profiles of the sublimated species. On the other hand, their scale heights are much bigger (on the order of several 1000 km), i.e., their density profiles fall off much shallower than the density profiles of the sublimated species. In fact, due to their much higher scale heights, sputtered CO, CO_2, N_2, H_2S, Ar, Na, K, PH_3, Kr, and Xe start to dominate their sublimated counterparts within Callisto's Hill radius. The fraction of escaping particles ranges from 4% for CH_4 to 100% for H, with most species exhibiting escape fractions of around 40% (Ar, CH_3OH, CO, CO_2, H_2O, K, N_2, Na, O, PH_3, and Xe), and only a few species making an exception (OH: ~15%, H_2S: ~20%, NH_3: ~30%, and Kr: ~70%). Due to the sputtered particles' on average longer flight times, the ionization rates of the sputtered particles are higher than of their sublimated counterparts. The ionization fractions are almost 10% for O, PH_3 and Xe, and a few percent each for CO_2, K, Na, and OH. Fragmentation also occurs a lot more frequently than in the sublimation case. Fragmentation affects around 50% of the CH_4, 30% each of the OH and H_2S, 20% of the NH_3, 10% of the CO_2 and 2% each of the CH_3OH and H_2O particles. Due to their already high initial velocity with addition of the gained dissociation energy, most fragments reach escape velocities during the break-up of the main molecule. Again, as for the sublimated species, the sputtered species are usually kept in order of their surface densities, with only H making an exception.

5.3. Sputtering of non-ice constituents

Sputtering of non-ice constituents leads, due to the low sputter yields, to low surface densities. Again, though, the particles' initial velocities are high (on average ~4 km/s compared to ~2 km/s for ice sputtered particles and ~440 m/s for sublimated particles), and their profiles thus rather shallow. Almost all O, H, Si, Mg, Fe, S, Na, Ni, C, Cr, Mn, P, Ti, Co, and N particles and about 85% of the K, 70% of the Ca, and half of the Al particles thus escape. On the other hand, ionization mainly affects the particles with the longest flight times, i.e., Al (50%), Ca (23%), K (5%), and O (4%). In addition, Si, Fe, Na, and C are ionized on a one percent level. The density profiles of the mineral sputtered particles are kept in their exact order as they appear on the surface.

5.4. Comparison to available measurements

As mentioned in Section 2.2, only few measurements regarding Callisto's atmospheric constituents are available. The only species directly observed in Callisto's exosphere is CO_2, with a surface number density of $N_0 \approx 4 \times 10^8\ \mathrm{cm}^{-3}$ and a vertical column density of $N_C \approx 8 \times 10^{14}\ \mathrm{cm}^{-2}$ measured at the equatorial noon region (Carlson, 1999). We compute again 10^5 CO_2 particles sublimating from Callisto's icy surface, this time at longitude of

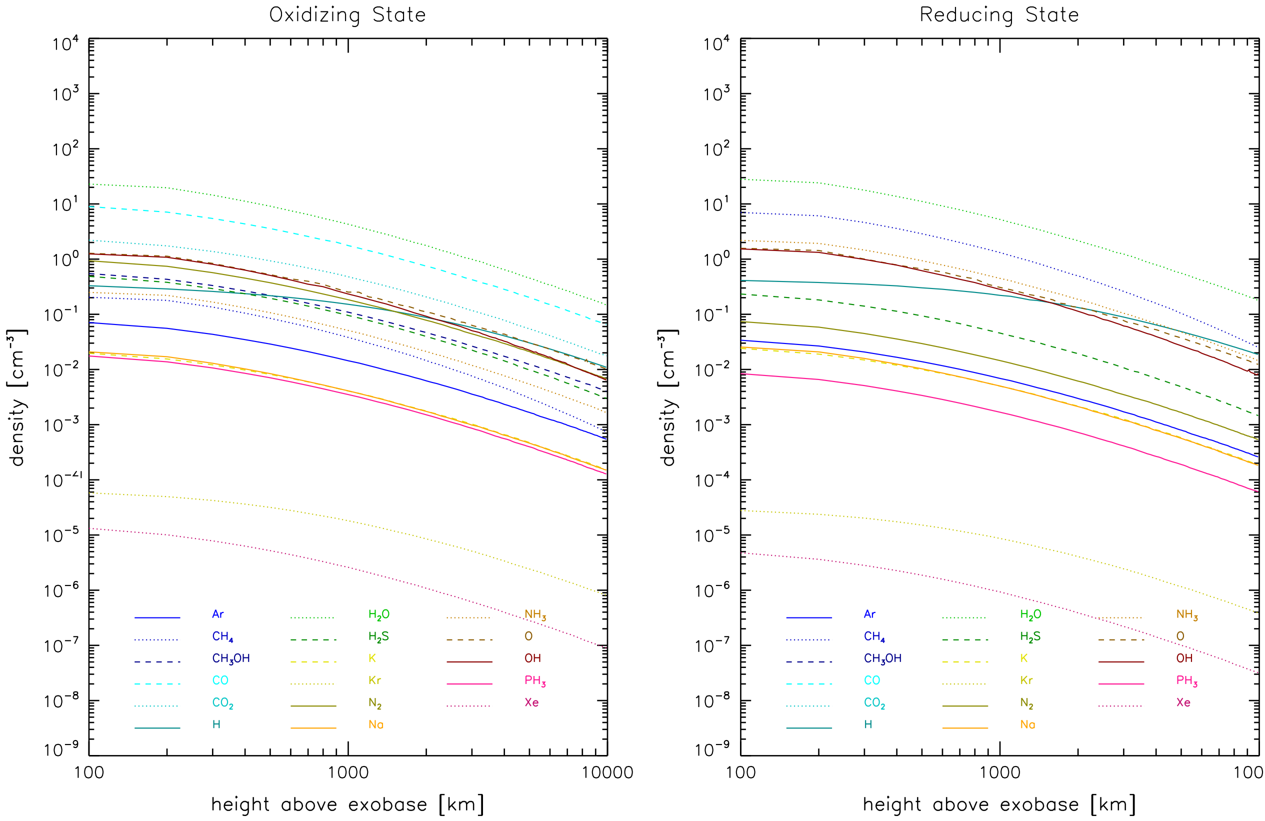

Fig. 4. Density profiles of particles that have been sputtered from Callisto's ice surface from the night side (sub-solar antipode). The left panel shows the results for a surface composition resembling the oxidizing state of the sub-nebula and the right panel shows the results for the ice composition resembling the reducing state of the sub-nebula. The density profiles contain the results for sputtering by magnetospheric H^+, O^{n+}, and S^{n+}.

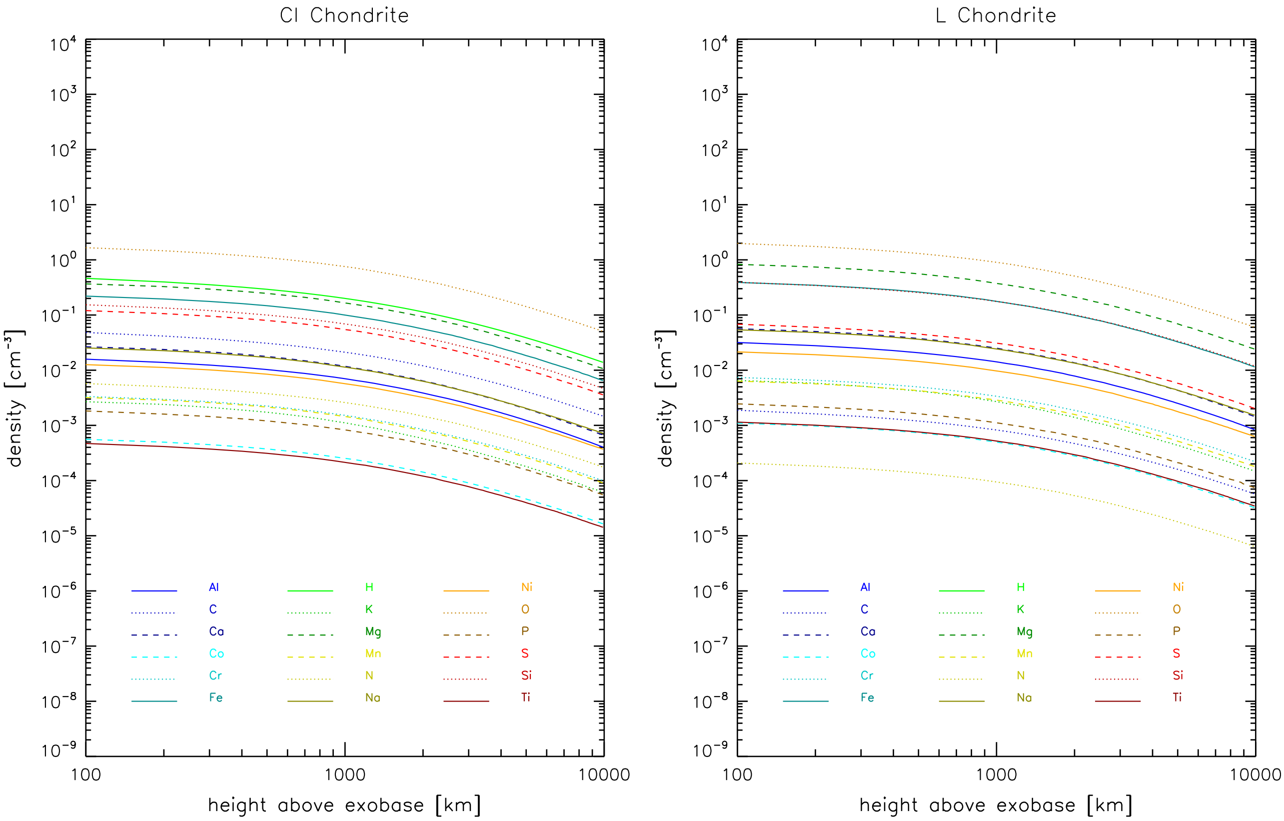

Fig. 5. Density profiles of particles that have been sputtered from Callisto's non-ice surface. The left panel shows the results for a surface compositions resembling the compositions of CI chondrites and the right panel shows the results for a surface composition resembling the composition of L chondrites.

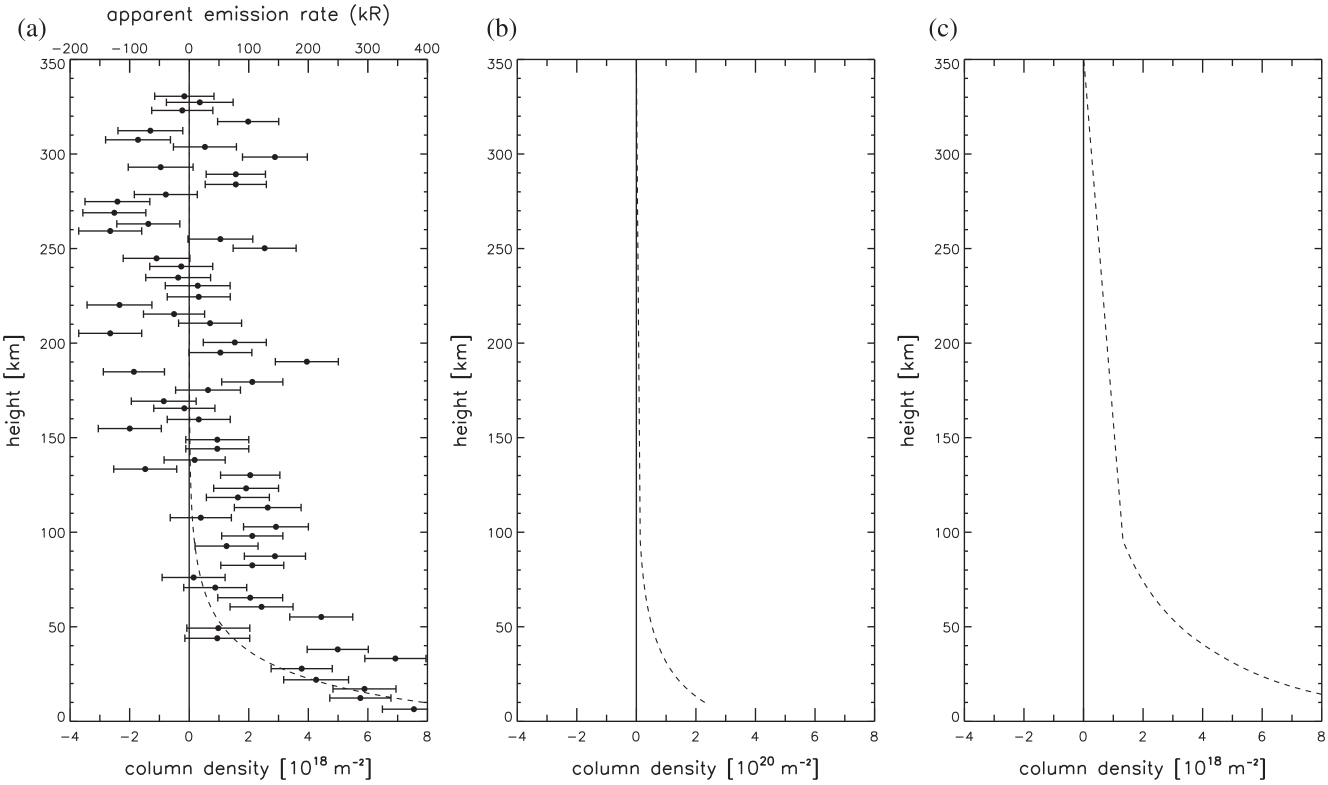

Fig. 6. Column density profiles for CO_2 (panel a), O_2 (panel b), and atomic O (panel c), each computed from 10^5 particles sublimating at a longitude of 120 deg. Also shown in panel a is the vertical CO_2 brightness computed by Carlson (1999) from Galileo NIMS data. Note the different ranges of the *x*-axes in the individual panels.

120 deg, which resembles the Carlson (1999) observational setting best. The resulting CO_2 column density is plotted in Fig. 6 panel a together with the vertical brightness profile presented in Carlson (1999) (Fig. 2b). Our computation results in a CO_2 scale height of $H \approx 19$ km (vs. 23 km in (Carlson, 1999)), a surface density of $N_0 \approx 2 \times 10^8$ cm^{-3} (vs. $\approx 4 \times 10^8$ cm^{-3} in (Carlson, 1999)) and a radial column density of $N_C \approx 4 \times 10^{14}$ cm^{-2} (vs. $\approx 8 \times 10^{14}$ cm^{-2} in Carlson (1999)). We would like to remind the reader that we assumed that the CO_2 sublimation is completely dominated by water ice sublimation (i.e., the CO_2 is well mixed with the water ice). This might of course only be valid to a certain degree; some of the CO_2 might in fact exist in pure form and thus sublimate on its own. All in all, our computation agree well with the Carlson (1999) measurements, considering their error interval of ±60%.

Regarding the O_2 densities, several density values are available for comparison. To fit Galileo ionosphere measurements, the surface number density was computed to be $N_0 = (1–3) \times 10^{10}$ cm^{-3} by Kliore et al. (2002), whereas the photochemical model presented by Liang et al. (2005) yielded a surface density of $N_0 = 7 \times 10^9$ cm^{-3}. Kliore et al. (2002) also give the surface column density value required to fit the Galileo ionosphere measurements, which is equal to $N_C = (3–4) \times 10^{16}$ cm^{-2}. Measurements conducted by the Hubble Space Telescope Cosmic Origins Spectrograph imply an O_2 column surface density of $N_C \approx 4 \times 10^{15}$ cm^{-2} for the leading hemisphere (Cunningham et al., 2015). The authors mention that the column surface density on the unobserved trailing hemisphere might be up to an order of magnitude larger. Our model yields a sub-solar surface density of $N_0 = 4.58 \times 10^9$ cm^{-3} and a night-side surface density of $N_0 = 7.04 \times 10^9$ cm^{-3}, assuming a surface column density of $N_C = 3 \times 10^{16}$ cm^{-2}. Fig. 6 also presents the column density profiles for O_2 (panel b) as well as atomic O (panel c), again for particles sublimating at a longitude of 120 deg (note the different ranges of the *x*-axes in the individual panels). With a radial O_2 column density of $N_C \approx 1 \times 10^{16}$ cm^{-2} these results also fit well within the range of the O_2 measurements.

5.5. NIM measurement capabilities

NIM is a neutral gas and ionospheric ion mass spectrometer specially designed to measure the chemical composition of exospheres during flyby and in orbit. The NIM design is based on an earlier instrument development for lunar research (Wurz et al., 2012). Fig. 7 shows three simulated mass spectra as they would be recorded by NIM during one of JUICE's Callisto flyby (integration time is 5 s). (Panel a) corresponds to an altitude of 10,000 km, (Panel b) corresponds to an altitude of 1000 km, and (Panel c) corresponds to an altitude of 200 km (closest approach). For this plot, the ice density profiles were taken from the computations for the oxidizing state and non-ice profiles were taken from the computations for material resembling CI chondrites. Shown are the mass spectra of the sublimated species (cyan), the ice-sputtered species (blue), the mineral-sputtered species (brown), and photon desorbed H_2O (magenta). The plots include all species' isotopes, with ratios between the isotopes computed from the species' representative isotopic compositions. NIM's expected detection threshold of 1 cm^{-3} for a 5-s integration due to instrument background is shown in black.

NIM, continuously sampling Callisto's exosphere during the spacecraft's approach, will be able to measure the density variations in the sublimated as well as the sputtered particles. Far away from Callisto, where the sputtered curves dominate the sublimated curves, the density increase with altitude decrease will be rather shallow. As soon as the sublimated particles start to dominate, though, the density profiles will increase rapidly.

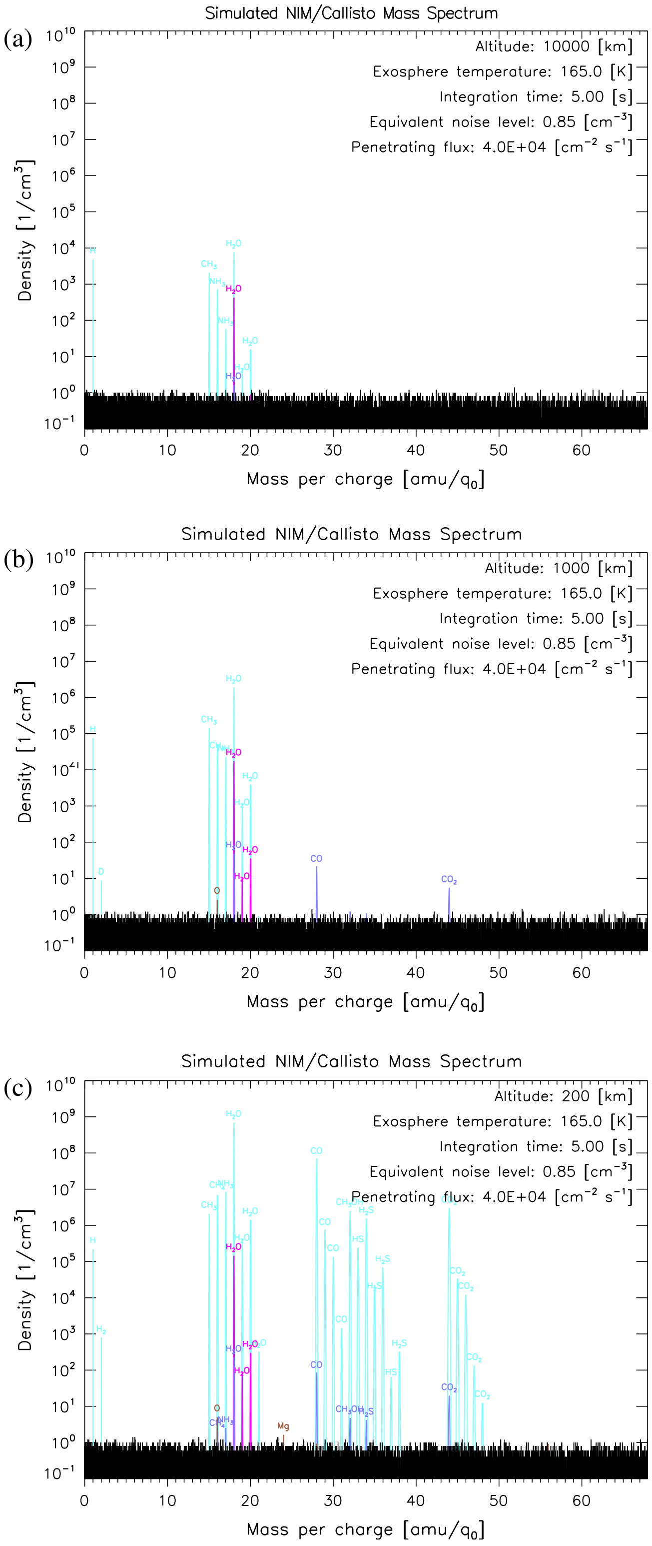

Fig. 7. Three example spectrograms as expected to be recorded by NIM during one of JUICE's Callisto flyby (integration time = 5 s). (Panel a) corresponds to a spacecraft altitude of 10,000 km, (Panel b) corresponds to a spacecraft altitude of 1000 km, and (Panel c) corresponds to a spacecraft altitude of 200 km (closest approach). The surface compositions resemble the oxidizing state of the sub-nebula for the ice surface and CI chondrites for the non-ice surface. Depicted are the spectra of the sublimated species (cyan), the ice-sputtered species (blue), the mineral-sputtered species (brown), and photon desorbed H_2O (magenta). Also shown is NIM's expected detection threshold of 1 cm^{-3} (instrument background) in black. In addition, for each peak detectable, the species that makes up the main part of the peak is denoted. (For interpretation of the references to colour in this figure legend, the reader is referred to the web version of this article.)

Measurements on Callisto's day-side at a few hundred kilometers will allow direct deduction of the ice surface composition, with even more exact results obtained when taking the species' scale heights into account. The main differences between the surface compositions corresponding to the oxidizing and the reducing state of the initial conditions in the sub-nebula are that for the oxidizing condition most of C is in CO and most of N is in N_2, whereas for the reducing condition all C is in CH_4 and most of N is in NH_3.

The mineral sputtered density profiles are very close to NIM's detection limit of 1 cm^{-3} for a 5-s integration period and it will be hard to detect most of the mineral sputtered species in such spectra. For favorable impinging plasma conditions (maximum speeds or densities; cf. Table 3) we can expect densities up to a factor 5 higher than shown in the plots. In addition, increasing NIM's integration time improves the signal to noise ratio by the square-root of the time increase, which lowers the background to 0.1 cm^{-3} by increasing the integration time accordingly. Summing up NIM's mass spectra or increasing its integration time should allow us thus to detect all main species present in the non-ice material.

6. Conclusion

Callisto possesses an extremely thin atmosphere, also called exosphere. So far, the only species directly observed in Callisto's atmosphere is CO_2. Measurements of an ionospheric layer above Callisto's sunlit trailing hemisphere showed, though, that CO_2 cannot be the most abundant species in Callisto's exosphere, as it is unable to account for the observed electron densities.

In this paper, we computed exospheric density profiles created ab initio from two different ice compositional models and two different non-ice compositional models. Since the ratio of the ice surface to the non-ice surface is not known (but commonly assumed to be about 1:1), we kept the density profiles of the two surface types separate. To represent the ice surface, we implemented two different compositional models, which are based on formation models of the Galilean moons. Both models represent two possible initial gas phase conditions in the solar nebula, the so-called oxidizing and reducing states. The main difference between the two models is that for the oxidizing condition most of C is in CO and most of N is in N_2, while for the reducing condition all C is in CH_4 and most of N is in NH_3. As for the non-ice surface, two different chondrite types exhibiting spectral properties similar to those observed on Callisto were chosen as composition representatives: CI and L chondrites. Release processes include sublimation, photon stimulated desorption and ion sputtering from the ice surface, and ion sputtering from the non-ice surface. Particles that enter Callisto's exosphere are either lost due to escape, due to ionization, due to fragmentation, or due to surface adsorption (after having returned to the surface).

Our simulations show that close to Callisto's surface the sublimated species strongly dominate the sputtered species. Surface densities at the sub-solar point sum up to $\sim 4 \cdot 10^{10}$ particles/cm^3, with H_2O, CO, CO_2 and O_2 making up the main part of the density for the oxidizing case, and H_2O, CH_4, O_2, and NH_3 making up the main part of the density of the reducing case. These high densities should allow to measure some isotope ratios, e.g., the D/H ratio in water. In comparison to ice-sputtered species, sublimated species have relatively low initial velocities, though, making their density profiles fall off rather rapidly. The only exception thereof are posed by the very light particles H and H_2. Ice-sputtered particles have much lower surface densities, but leave the surface at much higher velocities than their sublimated counterparts. Their density profiles thus drop off much shallower, and CO, CO_2, N_2, H_2S, Ar, Na, K, PH_3, Kr, and Xe start to dominate their sublimated counterparts within Callisto's Hill radius. Mineral-sputtered particles have surface densities even lower than ice-sputtered particles, but escape velocities about twice as high as the ice-sputtered particles' escape velocity. Their density curves are therefore the shallowest.

Particles that are ionized become part of Jupiter's magnetosphere as they are swept away by the electro-magnetic fields of the magnetosphere. The ion production rate Q (or ion entry rate into Jupiter's magnetosphere) not only takes the ionization rates into account, but of course also the surface densities (how many particles are available for ionization). The most significant ions originating from neutrals in Callisto's exosphere that enter Jupiter's magnetosphere are sublimated CO_2, CO, H_2O and CH_4. The most significant production rates of sputtered ions from the ice surface are $\sim 1 \cdot 10^{10}$ ions/s for O, $\sim 7 \cdot 10^9$ ions/s for CO_2, $\sim 4 \cdot 10^9$ ions/s for PH_3, and $\sim 1 \cdot 10^9$ ions/s for OH. The only mineral-sputtered species with a significant ion production rate are O with $\sim 7 \cdot 10^{11}$ ions/s, and Al and K, each with $\sim 1 \cdot 10^9$ ions/s.

There are a few potential caveats that we would like to mention here. First of all, our Monte-Carlo model computes density profiles based on surface density values. Assumptions about the ice and non-ice compositions therefore directly scale our density profiles. Concerning surface release processes, we assumed that the sublimation dynamics of all major species are dominated by the water ice sublimation. It is possible, though, that other ices besides water ice exist (e.g., CO_2-ice), and that these ices sublimate independently of the water ice. In addition, when computing sputter profiles, we assumed that the magnetospheric plasma can reach Callisto's surface almost unhindered, whereas in reality most probably only part of the plasma is able to reach Callisto's surface while the rest is diverted around the satellite. Since plasma densities themselves vary by more than an order of magnitude, though, we find our approach of taking the average plasma density into account and assuming full penetration a justified first approach. Concerning loss processes, the ionization losses are probably the most uncertain. Ionization losses include photo-ionization, magnetospheric electron ionization, and charge exchange with magnetospheric ions. Currently our model only takes the first two ionization losses processes into account. Finally, and most notably, our simulation approach is based on the assumption that the particles travel on unhindered trajectories. Since very recent observations (published while this paper was under revision) imply that Callisto's exosphere might in fact not be an exosphere at all, but rather a collisional atmosphere, a follow-up study should re-evaluate the validity of our approach. This study will have to determine what influence a collisional layer close to the surface might have on our density profiles, and for which particles and release processes our assumption of an exobase located at the surface is justifiable. If the exobase turns out to be indeed located at a certain distance from the satellites surface, and if it turns out that some particle's density profiles are thereby influenced, we might have to re-run our simulations for these particles with the newly gained information.

Thanks to NIM's high mass resolution, NIM will be able to measure all sublimated species and to distinguish between the oxidizing and the reducing case of the ice surface composition, mainly by observing the presence/absence of CO and CO_2 and by determining the N_2 to NH_3 ratio. In addition, due to the instrument's high sensitivity, NIM will be able to distinguish between the sublimated and sputtered particles originating from the ice surface by rapid sampling of the density curves during the flight: While sublimated particles start at much higher densities, their density profiles fall off much faster with altitude. Even with the conservative estimate shown in Fig. 7, NIM should be able to measure at least some of the species sputtered from the minerals. For favorable magnetic plasma conditions and by increasing NIM's integration time the signal to noise ratio can be increased by a few orders. NIM should thus also be capable to distinguish between the different non-ice compositional models. Overall, based on NIM measurements we should be able to determine what species are present to what degree in Callisto's ice and non-ice surface, and to identify the compositional model best matching the these surface abundances.

References

Alibert, Y., Mousis, O., 2007. Formation of Titan in Saturn's subnebula: Constraints from Huygens probe measurements. Astron. Astrophys. 465, 1051–1060. http://dx.doi.org/10.1051/0004-6361:20066402.

Alibert, Y. et al., 2005a. Models of giant planet formation with migration and disc evolution. Astron. Astrophys. 434, 343–353.

Alibert, Y., Mousis, O., Benz, W., 2005b. Modeling the jovian subnebula: I. Thermodynamic conditions and migration of proto-satellites. Astron. Astrophys. 439, 1205–1213.

Alibert, Y. et al., 2013. Theoretical models of planetary system formation: Mass vs. semi-major axis. Astron. Astrophys. 558, A109.

Bagenal, F., 2004. Jupiter's Magnetosphere: Coupling the Equator to the Poles. AGU Fall Meeting Abstracts, p. A1.

Bagenal, F. et al., 1992. The abundance of O^{++} in the jovian magnetosphere. Geophys. Res. Lett. 19 (2), 79–82.

Barabash, S. et al., 2013. Particle Environment Package (PEP). European Planetary Science Congress 2013, held 8–13 September in London, UK, vol. 8. EPSC2013.

Calvin, W.M., Clark, R.N., 1991. Modeling the Reflectance Spectrum of Callisto 0.25 to 4.1 μm. Icarus 89, 305–317.

Calvin, W.M. et al., 1995. Spectra of the icy Galilean satellites from 0.2 to 5 μm: A compilation, new observations, and a recent summary. J. Geophys. Res., 100(E9)

Canup, R.M., Ward, W.R., 2002. Formation of the Galilean Satellites: Conditions of accretion. Astron. J. 124, 3404–3423. http://dx.doi.org/10.1086/344684.

Canup, R.M., Ward, W.R., 2006. A common mass scaling for satellite systems of gaseous planets. Nature 441, 834–839. http://dx.doi.org/10.1038/nature04860.

Carlson, R.W., 1999. A tenuous carbon dioxide atmosphere on Jupiter's moon Callisto. Science 283 (820). http://dx.doi.org/10.1126/science.283.5403.820.

Carlson, R. et al., 1996. Near-infrared spectroscopy and spectral mapping of Jupiter and the Galilean satellites: Results from Galileo's initial orbit. Science 274, 385–388.

Cassidy, T. et al., 2010. Radiolysis and photolysis of icy satellite surfaces: Experiments and theory. Space Sci. Rev. 153, 299–315. http://dx.doi.org/10.1007/s11214-009-9625-3.

Cooper, J.F. et al., 2001. Energetic ion and electron irradiation of the icy Galilean satellites. Icarus 149, 133–159. http://dx.doi.org/10.1006/icar.2000.6498.

Coradini, A., Magni, G., 1984. Structure of the satelitary accretion disk of Saturn. Icarus 59, 376–391. http://dx.doi.org/10.1016/0019-1035(84)90108-8.

Cunningham, N.J. et al., 2015. Detection of Callisto's oxygen atmosphere with the Hubble Space Telescope. Icarus 254, 178–189. http://dx.doi.org/10.1016/j.icarus.2015.03.021.

Famá, M., Shi, J., Baragiola, R.A., 2008. Sputtering of ice by low-energy ions. Surface Sci. 602, 156–161. http://dx.doi.org/10.1016/j.susc.2007.10.002.

Frank, L.A., Paterson, W.R., Khurana, K.K., 2002. Observations of thermal plasmas in Jupiter's magnetotail. J. Geophys. Res. 107 (A1). http://dx.doi.org/10.1029/2001JA000077.

Fray, N., Schmitt, B., 2009. Sublimation of ices of astrophysical interest: A bibliographic review. Planet. Space Sci. 57, 2053–2080. http://dx.doi.org/10.1016/j.pss.2009.09.011.

Galli, A. et al., 2015. A new laboratory facility for studying surface erosion and atmosphere production processes of the icy moons of Jupiter, Icarus (submitted for publication).

Gladstone, R. et al., 2013. The Ultraviolet Spectrograph (UVS) on ESA's JUICE Mission. European Planetary Science Congress 2013, held 8–13 September in London, UK, vol. 8. EPSC2013.

Grasset, O. et al., 2013. JUpiter ICy moons Explorer (JUICE): An ESA mission to orbit Ganymede and to characterise the Jupiter system. Planet. Space Sci. 78, 1–21. http://dx.doi.org/10.1016/j.pss.2012.12.002.

Greeley, R. et al., 2000. Galileo views of the geology of Callisto. Planet. Space Sci. 48, 829–853.

Hartogh, P. et al., 2013. The Submillimetre Wave Instrument on JUICE. European Planetary Science Congress 2013, held 8–13 September in London, UK, vol. 8. EPSC2013.

Hibbitts, C.A., McCord, T.B., Hansen, G.B., 2000. Distributions of CO_2 and SO_2 on the surface of Callisto. J. Geophys. Res. 105 (E9). http://dx.doi.org/10.1029/1999JE001101.

Horner, J. et al., 2008. Constraints from deuterium on the formation of icy bodies in the jovian system and beyond. Planet. Space Sci. 56, 1585–1595. http://dx.doi.org/10.1016/j.pss.2008.04.010.

Huebner, W.F., Keady, J.J., Lyon, S.P., 1992. Solar photo rates for planetary atmospheres and atmospheric pollutants. Astrophys. Space Sci. 195 (1), 1–294.

Johnson, R.E. et al., 2002. Energy distributions for desorption of sodium and potassium from ice: The Na/K ratio at Europa. Icarus 156, 136–142. http://dx.doi.org/10.1006/icar.2001.6763.

Johnson, T.V. et al., 2012. Planetesimal compositions in exoplanet systems. Astron. Astrophys. 757 (192). http://dx.doi.org/10.1088/0004-637X/757/2/192.

Jursa, A.S. (Ed.), 1985. Handbook of Geophysics and the Space Environment, fourth ed. Air Force Geophysics Laboratory, Hanscom, MA, USA.

Kavelaars, J.J. et al., 2011. On the formation location of Uranus and Neptune as constrained by dynamical and chemical models of comets. Astrophys. J. 734, L30. http://dx.doi.org/10.1088/2041-8205/734/2/L30.

Killen, R. et al., 2007. Processes that promote and deplete the exosphere of Mercury. Space Sci. Rev. 132, 433–509.

Kivelson, M.G. et al., 2007. Jupiter: The Planet, Satellites and Magnetosphere, vol. 1. Cambridge University Press, pp. 513–536 (Chapter 21).

Kliore, A.J. et al., 2002. Ionosphere of Callisto from Galileo radio occultation observations. J. Geophys. Res. 107 (A11). http://dx.doi.org/10.1029/2002JA009365.

Kuskov, O.L., Kronrod, V.A., 2001. Core size and internal structure of Earth's and Jupiter's satellites. Icarus 151, 204–227. http://dx.doi.org/10.1006/icar.2001.6611.

Kuskov, O.L., Kronrod, V.A., 2005. Internal structure of Europa and Callisto. Icarus 177, 550–569. http://dx.doi.org/10.1016/j.icarus.2005.04.014.

Küstner, M. et al., 1998. The influence of surface roughness on the angular dependence of the sputter yield. Nucl. Instrum. Methods Phys. Res. B 145, 320–331.

Langevin, Y. et al., 2013. MAJIS (Moons And Jupiter Imaging Spectrometer) for JUICE: Objectives for the Galilean satellites. European Planetary Science Congress 2013, held 8–13 September in London, UK, vol. 8. EPSC2013.

Liang, M.-C. et al., 2005. Atmosphere of Callisto. J. Geophys. Res. 110 (E02003). http://dx.doi.org/10.1029/2004JE002322.

Lubow, S.H., Seibert, M., Artymowicz, P., 1999. Disk accretion onto high-mass planets. Astrophys. J. 526, 1001–1012. http://dx.doi.org/10.1086/308045.

Marconi, M.L., 2007. A kinetic model of Ganymede's atmosphere. Icarus 190, 155–174. http://dx.doi.org/10.1016/j.icarus.2007.02.016.

McCord, T.B. et al., 1998. Non-water-ice constituents in the surface material of the icy Galilean satellites from the Galileo near-infrared mapping spectrometer investigation. J. Geophys. Res. 103 (E4), 8603–8626. http://dx.doi.org/10.1029/98JE00788.

Moore, J.M. et al., 2004. Jupiter: The planet, satellites and magnetosphere. Cambridge Planetary Science, vol. 1. Cambridge University Press, Cambridge, UK, pp. 397–426.

Mordasini, C. et al., 2014. Global models of planet formation and evolution. Int. J. Astrobiol. 12, 201–232.

Mousis, O., Alibert, Y., 2006. Modeling the jovian subnebula – II. Composition of regular satellite ices. Astron. Astrophys. 448 (L7), 771–778. http://dx.doi.org/10.1051/0004-6361:20053211.

Mousis, O., Gautier, D., 2004. Constraints on the presence of volatiles in Ganymede and Callisto from an evolutionary turbulent model of the jovian subnebula. Planet. Space Sci. 52, 361–370. http://dx.doi.org/10.1016/j.pss.2003.06.004.

Mousis, O. et al., 2009. Clathration of Volatiles in the Solar Nebula and Implications for the Origin of Titan's atmosphere. Astrophys. J. 691, 1780–1786. http://dx.doi.org/10.1088/0004-637X/691/2/1780.

Mousis, O. et al., 2012. Nebular water depletion as the cause of Jupiter's low oxygen abundance. Astrophys. J. 751 (L7). http://dx.doi.org/10.1088/2041-8205/751/1/L7.

Nagel, K., Breuer, D., Spohn, T., 2004. A model for the interior structure, evolution, and differentiation of Callisto. Icarus 169, 402–412. http://dx.doi.org/10.1016/j.icarus.2003.12.019.

Pasek, M.A. et al., 2005. Sulfur chemistry with time-varying oxygen abundance during Solar System formation. Icarus 175, 1–14. http://dx.doi.org/10.1016/j.icarus.2004.10.012.

Pollack, J.B. et al., 1996. Formation of the giant planets by concurrent accretion of solids and gas. Icarus 124, 62–85. http://dx.doi.org/10.1006/icar.1996.0190.

Prinn, R.G., Fegley Jr., B., 1981. Kinetic inhibition of CO and N_2 reduction in circumplanetary nebulae – Implications for satellite composition. Astrophys. J. 249, 308–317. http://dx.doi.org/10.1086/159289.

Prinn, R.G.P., Fegley Jr., B., 1989. Solar nebula chemistry: Origins of planetary, satellite and cometary volatiles, 78–136.

Schaufelberger, A. et al., 2011. Scattering function for energetic neutral hydrogen atoms off the lunar surface. Geophys. Res. Lett. 38 (L22202). http://dx.doi.org/10.1029/2011GL049362.

Schubert, G. et al., 2010. Evolution of icy satellites. Space Sci. Rev. 153, 447–484. http://dx.doi.org/10.1007/s11214-010-9635-1.

Shematovich, V.I. et al., 2005. Surface-bounded atmosphere of Europa. Icarus 173, 480–493.

Shi, M. et al., 1995. Sputtering of water ice surfaces and the production of extended neutral atmospheres. J. Geophys. Res. 100 (E12), 26387–26396.

Showman, A.P., Malhotra, R., 1999. The Galilean satellites. Science, 286.

Smith, B.A. et al., 1979. The Galilean satellites and Jupiter: Voyager 2 imaging science results. Science. Article No: 206. pp. 927–950.

Spencer, J.R., Calvin, W.M., 2002. Condensed O_2 on Europa and Callisto. Astrophys. J. 124, 3400–3403.

Stebbins, J., Jacobsen, T.S., 1928. Further photometric measures of Jupiter's satellites and Uranus, with tests of the solar constant. Lick Observatory Bull. Article No: 401. pp. 180–195.

Strobel, D.F. et al., 2002. Hubble space telescope space telescope imaging spectograph search for an atmosphere on Callisto: A jovian unipolar inductor. Astrophys. J. 581, 51–54.

Wahlund, J.-E. et al., 2013. The Radio and Plasma Wave Investigation (RPWI) for JUICE. European Planetary Science Congress 2013, held 8–13 September in London, UK, vol. 8. EPSC2013.

Waite Jr., J.H. et al., 2009. Liquid water on Enceladus from observations of ammonia and ^{40}Ar in the plume. Nature 460, 487–490. http://dx.doi.org/10.1038/nature08153.

Wasson, J.T., Kallemeyn, G.W., 1988. Compositions of Chondrites. R. Soc. London Philos. Trans. Ser. A 325, 535–544.

Westley, M.S., Baragiola, R.E.J.R.A., Baratta, G.A., 1995. Photodesorption from low-temperature water ice in interstellar and circumsolar grains. Nature. Article No: 373. pp. 405–407.

Wurz, P., Lammer, H., 2003. Monte-Carlo simulation of Mercurys exosphere. Icarus 164, 1–13. http://dx.doi.org/10.1016/S0019-1035(03)00123-4.

Wurz, P. et al., 2007. The lunar exosphere: The sputtering contribution. Icarus 191, 486–496. http://dx.doi.org/10.1016/j.icarus.2007.04.034.

Wurz, P. et al., 2010. Self-consistent modelling of Mercurys exosphere by sputtering, micro-meteorite impact and photon-stimulated desorption, Planet. Space Sci. 58, 1599–1616. http://dx.doi.org/10.1016/j.pss.2010.08.003.

Wurz, P. et al., 2012. A neutral gas mass spectrometer for the investigation of lunar volatiles. Planet. Space Sci. 74, 264–269. http://dx.doi.org/10.1016/j.pss.2012.05.016.

Zimmer, C., Khurana, K.K., Kivelson, M.G., 2000. Subsurface oceans on Europa and Callisto: Constraints from Galileo magnetometer observations. Icarus 147, 329–347. http://dx.doi.org/10.1006/icar.2000.6456.